GPS Measurements of Precipitable Water Vapor Can Improve Survey Calibration: A Demonstration from KPNO and the Mayall z-band Legacy Survey

W. M. Wood-Vasey,[1] Daniel Perrefort,[1] and Ashley D. Baker[2,3]

[1] Pittsburgh Particle Physics, Astrophysics, and Cosmology Center (PITT PACC). Physics and Astronomy Department, University of Pittsburgh, Pittsburgh, PA 15260, USA
[2] University of Pennsylvania Department of Physics and Astronomy. 209 S 33rd Street, Philadelphia, PA 19104, USA
[3] Department of Astronomy, California Institute of Technology, Pasadena, CA 91125, USA

ABSTRACT

Accounting for the effects of atmospheric absorption is a key step in calibrating high-accuracy photometry. In particular, the atmospheric transmission redward of 550 nm is dominated by absorption due to water vapor. We here show that dual-band GPS measurements of precipitable water vapor (PWV) at the Kitt Peak National Observatory (KPNO) predict the overall per-image sensitivity of the Mayall z-band Legacy Survey (MzLS). We further find that the per-image variation in the brightness of individual stars is strongly correlated with the measured PWV and the color of the star. We use synthetic stellar spectra and TAPAS transmission models to predict the expected PWV-induced photometric errors and find good agreement with the observations. In line with previous work in the literature we also find that PWV absorption can be well-approximated by a linear relationship with $\mathrm{PWV}^{\mathrm{eff}}_{\mathrm{los}}$ and present an update on the traditional treatment in the literature.

Within the range of reasonable observing conditions, the MzLS zero point varies with a standard deviation of 127 mmag. This variation is dominated by a gray secular trend with time, consistent with a gradual accumulation of contamination on optical surfaces that accounts for $\sim$114 mmag of variation. Correcting for PWV based on a suite of stellar spectra and detailed PWV absorption models accounts for another 47 mmag of zero-point variation. The MzLS per-image sensitivity is decreased by $\sim$40 mmag per effective mm of PWV. The difference between blue ($r - z < 0.5$ mag) and red (1.2 mag $< r - z$) stars increases by 3.25 mmag per effective mm of PWV.

These results show the need for high-precision photometric surveys to simultaneously monitor PWV. We find that GPS systems provide more precise PWV measurements than using differential measurements of stars of different colors and recommend that observatories that observe long-ward of 800 nm install dual-band GPS as a low-maintenance, relatively low cost, auxiliary calibration system. We extend our results of the need for well-calibrated PWV measurements by presenting calculations of the PWV photometric impact on three science cases of interest: stellar photometry, supernova cosmology, and quasar identification and variability.

1. INTRODUCTION

Modern astronomical surveys such as the Dark Energy Survey (DES; Dark Energy Survey Collaboration et al. 2016) and the Panoramic Survey Telescope and Rapid Response System (Pan-STARRS; Magnier et al. 2016) require high photometric accuracy, and upcoming surveys such as the Vera Rubin Observatory Legacy Survey of Space and Time (LSST; Ivezić et al. 2019) will strive to push this limit even further by requiring a 5 mmag photometric accuracy. For surveys relying on ground-based telescopes, accounting and correcting for effects induced by the Earth's atmosphere is a key step in achieving this goal (see Ivezić et al. 2007; Magnier et al. 2016; Burke et al. 2010, 2014; Burke et al. 2018). In particular, absorption features due to the presence of water vapor dominate the atmospheric transmission function in the red optical and near-infrared (NIR) band-passes ($\lambda > 550$ nm). The complicated yet known structure of water vapor absorption must be accurately and precisely accounted for to accurately determine the complete system throughput as a function of wavelength.

Broad-band imaging is traditionally calibrated using a reference catalog to compute correction terms for color, airmass, and a higher-order color-airmass term. While this approach implicitly corrects for first-order effects introduced by the atmospheric opacity, it does not account for second-order effects caused by differences in the atmospheric absorption between the spectral energy distributions of the target and reference stars. Because redder stars emit much more of their light at wavelengths susceptible to atmospheric absorption, their photometric values vary differently than bluer stars with changes in atmospheric conditions. This difference in behavior can introduce second-order photometric errors of over 1% (Ivezić et al. 2007; Li et al. 2016), which is significant in an era of high-accuracy photometry.

Approaches that allow for time-dependent color terms can account for time-variable absorption. However, these color terms work best where the differences in the SEDs can be described by smooth monotonic functions, such as in the Rayleigh-Jeans tail of the effective blackbody approximation for K-type and hotter stars. This approach works particularly well for effects that themselves are smooth in wavelength, such as Mie scattering due to atmospheric aerosols. However, the contribution to the atmospheric absorption due to atmospheric water vapor is not smooth.

Unlike the attenuation of light due to ozone and aerosols, absorption due to precipitable water vapor (PWV) has a complex transmission function with lines that saturate even during relatively dry and *photometric* conditions (PWV ≈ 5 mm). The convention is to measure water vapor in units of the mm of liquid water if it were all condensed. Local PWV concentrations can change by up to 10% per hour (Li et al. 2017), requiring a photometric correction that varies over the course of an observing night. Correctly accounting for variable complex atmospheric transmission requires a detailed understanding of the atmospheric state during the time in which observations were performed.

A common astronomical method for quantifying the absorption due to the atmosphere is to perform dedicated observations of a young A-type star (e.g., as in Stubbs et al. 2007). Because these stars have relatively few intrinsic features and are well described by existing models, the effects of atmospheric absorption can be fit for using forward modeling. When performed spectroscopically, fitting these observations provides a detailed map of the per-wavelength transmission of the atmosphere. This approach can also be performed photometrically by using narrow-band filters centered on key atmospheric features (Li et al. 2014; Baker et al. 2017). This narrow-band image approach benefits from the ability to perform in situ measurements along a similar line of sight to the scientific obser-

vations. Both of these approaches require the maintenance and calibration of a secondary, dedicated telescope.

An alternative method to measure the water absorption is to use dual-band receivers tracking signals from Global Positioning Satellites (GPS). By measuring the delay of dual-band GPS signals traveling through the atmosphere, it is possible to determine the PWV column density along zenith (Nahmias & Zabransky 2004; Blake & Shaw 2011; Manandhar et al. 2018). Through the use of atmospheric models and scaling relations, the atmospheric transmission due to PWV can be determined for the line-of-sight airmass of a given observation. This approach benefits from the ability to perform atmospheric measurements in near real-time and results in values that correlate strongly with spectroscopic measurements (Li et al. 2017). However, GPS measurements tend to be less accurate in dry conditions (Buehler et al. 2012; Hagemann et al. 2003) and cannot constrain the transmission due to secondary (non-PWV) components of the atmosphere.

In this work, we demonstrate the effect of PWV on the measured zero points and color-dependent per-image offsets using observations taken by the Mayall z-band Legacy Survey (MzLS) combined with contemporaneous GPS PWV measurements from Kitt Peak National Observatory (KPNO).

In Section 2 we outline the MzLS observations (2.1), PWV measurements (2.2), and atmospheric models (2.3) considered by this work. In Section 3 we demonstrate the effects of PWV absorption on MzLS zero points and compare using GPS-measured PWV to using the differential brightness of stars of different colors to predict zero point variation. We then consider the impact of PWV on various science cases in Section 5, including the impact on stars (5.1), supernovae (5.2), and quasars (5.3). Finally, we discuss the application of PWV measurement techniques to upcoming surveys in Section 6.

2. DATA

2.1. *Mayall z-band Legacy Survey*

The Mayall z-band Legacy Survey (MzLS) is one of the three public surveys that comprised the DESI Legacy Imaging Surveys[1] (Dey et al. 2019). Using the Mosaic-3 camera on the 4-meter Mayall telescope at Kitt Peak National Observatory (KPNO) (Dey & Valdes 2014; Dey et al. 2016), MzLS observed approximately $5,100\,\mathrm{deg}^2$ of the sky in the z-band. Mosaic-3 represents a significant upgrade from the Mosaic-1 and Mosaic-2 cameras (Dey & Valdes 2014), with a 500 μm thick CCD that significantly increased the quantum efficiency out to 1 μm. The z-band Mosaic-3 filter, shown in Figure 1, was chosen to be very similar to the z-band filter of the Dark Energy Camera (DECam Flaugher et al. 2015) on the CTIO 4 m Blanco telescope to allow for standard comparisons across hemispheres. After a commissioning phase for Mosaic-3 from 2015 October–December, the MzLS survey formally ran from 2016 February 2 through 2018 February 12. There are 60,431 exposures recorded in the MzLS archive, with 60,403 exposures with a non-zero recorded zero point.

In order to increase the observable depth, MzLS used a 3-pass strategy to tile the sky (Burleigh et al. 2020). To ensure the accurate calibration of each exposure, the first pass of observations were performed exclusively under two conditions; clear skies with a transparency $\geq 90\%$, and a seeing better than $1.3''$. The second pass was performed when at least one of these conditions were met, and the third pass was performed with no requirements. This approach guaranteed at least one
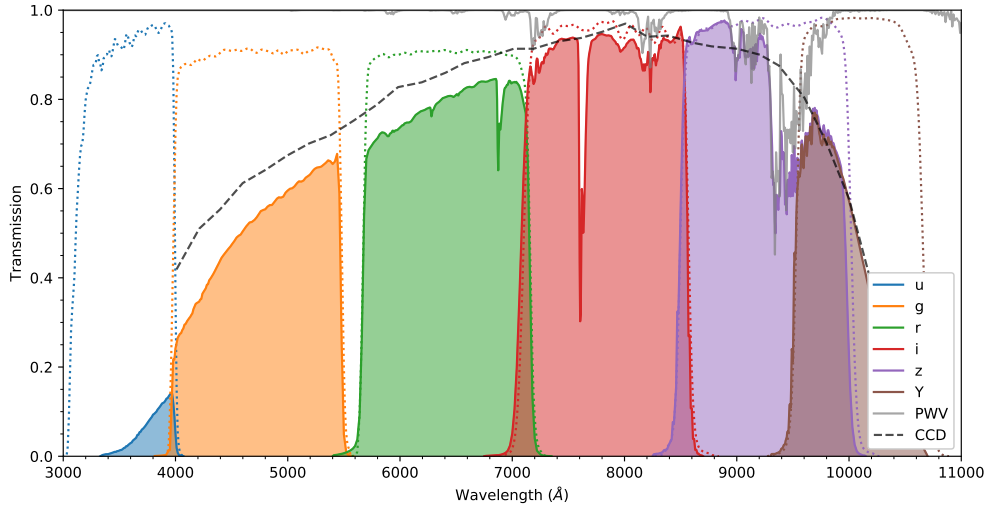
---

[1] http://legacysurvey.org

Figure 1. The optical throughput of DECam in the $ugrizY$ band-passes. The MzLS z-band filter is the same design as the DECam filter. Absorption due to PWV (solid gray) is for a fiducial atmosphere over KPNO (PWV $\approx$ 4 mm) in addition to the QE response of the CCD (dashed black). The transmission from these components is multiplied with the transmission of each optical filter (dotted) to determine the transmission of each individual band-pass (shaded). The filter transmission and detector QE are smooth, but PWV absorption completely determines the sensitivity in the red half of the z-band filter. The i-band transmission is also affected by PWV absorption, but the effect is a significantly smaller fraction of the transmission.

high-quality observation at each location in the sky that can be used to calibrate the photometry across the entire survey footprint.

MzLS observations taken during the second and third passes were calibrated by directly matching to overlapping observations taken during the first pass. The zero points were then determined individually for each CCD by measuring the instrumental magnitude of each source and matching the source to photometry from the first Pan-STARRS data release (PS1 DR1; Schlafly et al. 2012). To facilitate this comparison, a subset of PS1 DR1 sources were selected as calibrators and their colors were compared empirically to create a map between the PS1 and MzLS instrumental systems (Dey et al. 2019, Eq. 6). Thus while the MzLS natural system itself is absolutely calibrated to PS1, the individual image-by-image zero points are in the MzLS natural system.

2.2. PWV

In 2015 March, we installed a dual-band GPS receiver on the WIYN 3.5 meter telescope building at KPNO to monitor the local PWV column density (Perrefort et al. 2019). Estimation of the PWV concentration from the resulting meteorological data is provided by the SuomiNet project (Ware et al. 2000). With the addition of pressure, temperature, and relative humidity measurements, SuomiNet estimates the PWV column density at zenith by measuring the delay of dual-band GPS signals traveling through the atmosphere. For KPNO, these values are compiled by SuomiNet at thirty-minute intervals.

The application of GPS receivers to monitor PWV works by measuring the relative phase shift between two GPS frequencies emitted through the atmosphere (for details on the methods, see Bevis
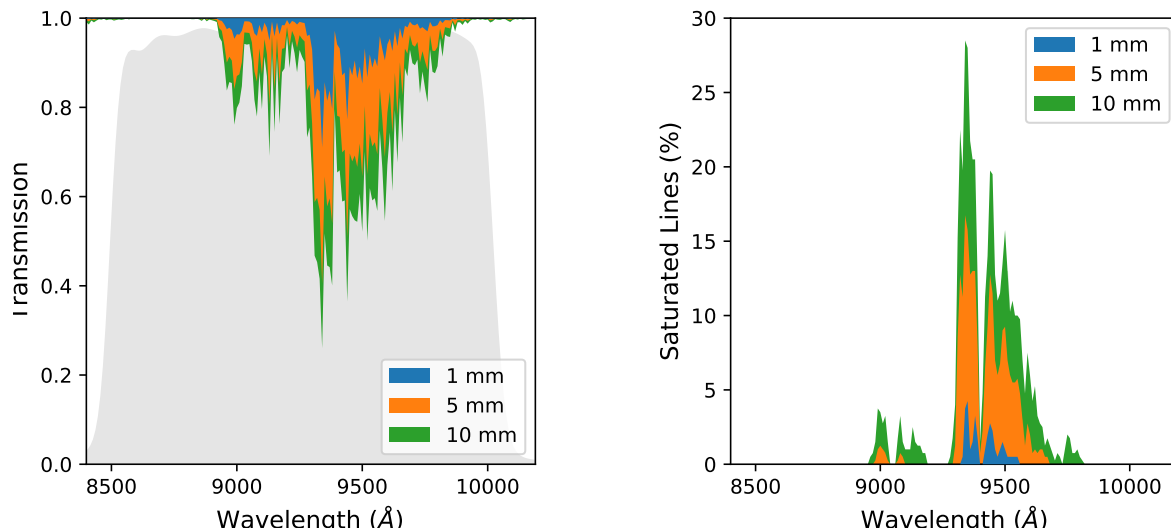
Figure 2. (left) the modeled atmospheric transmission due to PWV for 1 mm (blue), 5 mm (orange), and 10 mm (green) of PWV along line of sight. (gray) the MzLS z-band filter response. As the PWV concentration increases, PWV absorption lines begin to saturate. (right) percentage of saturated lines as a function of wavelength using a 0.05 nm resolution atmospheric model for each PWV concentration.

et al. 1994, 1992). The magnitude of the delay imposed on each signal is directly related to the frequency-dependent index of refraction along the optical path. This delay, known as the Zenith Total Delay, can be separated into a wet (PWV driven) and dry (non-PWV) component through the use of atmospheric models (Tralli & Lichten 1990). Although this approach is a recent advent in astronomy (Braun & Hove 2001; Dumont & Zabransky 2001; Nahmias & Zabransky 2004; Blake & Shaw 2011), the use of GPS to measure PWV has a longer history in meteorology (Bevis et al. 1992) and has undergone continual improvement with a focus on minimizing the estimated uncertainty, often achieving levels ≤ 2 mm (Moore et al. 2015; Shangguan et al. 2015; Sapucci et al. 2019).

From 2016 January through March, the barometric sensor at KPNO malfunctioned intermittently. This caused successive non-physical spikes in PWV estimates measured during this period. To avoid propagating these errors into this work, we ignore any PWV measurements taken over this three month period. This removes $\sim$10,000 of the main-survey MzLS exposures. Table 1 details the number of exposures for subsets of the MzLS survey relevant for this work. Figure 3 shows the distribution of airmass, MJD, and zero point for the MzLS survey along with the PWV$_{\text{zenith}}$ values measured from the KPNO dual-band GPS. PWV$_{\text{zenith}}$ values are comparable across the seasons, although 2017B started with a particularly high PWV$_{\text{zenith}}$ during the monsoon season. However, the airmass values in the 2017B season were significantly higher because the MzLS region extends from 100<RA<300 degrees and so observations made in the second half of the year have to reach over to access the MzLS region. Once the full MzLS region became more visible in the last part of 2017B, the airmass of the observations came back down.

2.3. *Telluric Transmission Models*

To manage data access for GPS measurements taken at KPNO, and to simulate the PWV transmission function, we use the `pwv_kpno` Python package (Perrefort et al. 2019). Using the wavelength

Table 1. MzLS Exposure Counting

Set	Number of MzLS Exposures
MzLS Survey + Commissioning	60,431
MzLS Survey	59,552
MzLS Survey in 2016A, 2017A, 2017B	56,646
MzLS Survey with KPNO PWV	49,321
$25.75 <$ zero point < 26.75 mag	57,243
"Clean": $25.75 <$ zero point < 26.75 mag in 2016A, 2017A, 2017B with KPNO PWV	43,373

dependent cross-section of atmospheric H_2O from MODTRAN (Berk et al. 2014), `pwv_kpno` scales the atmospheric transmission function according to the effective PWV concentration along line of sight. The model provides simulations exclusively for PWV absorption, and does not include effects introduced by other atmospheric components. In Figure 2 in the left panel, the water vapor transmission model for 1, 5, and 10 mm values of PWV are plotted over the MzLS z-band. In the right panel of Figure 2 we show the percent of saturated lines as a function of wavelength.

To model Rayleigh scattering and oxygen absorption, we use the TAPAS web service (Bertaux et al. 2014) to generate the atmospheric transmission function for KPNO at an airmass of 1. This PWV absorption spectrum is effectively identical to the one using pwv_kpno once scaled to the same PWV value.

3. RESULTS FROM MZLS

We here analyze the dependency of the MzLS zero points and per-epoch variations in inferred magnitudes of stars as a function of their color and PWV. Section 3.2 describes the MzLS zero points and discusses how the main contribution is a gray secular trend consistent with dust accumulation on the optical surfaces. Section 3.3 presents that the majority of the remaining zero-point variation is well-explained by the GPS-measured PWV at KPNO. Section 3.4 confirms that the effects of the long-term secular MJD trend and the PWV variation are largely separable. Section 3.5 examines the per-epoch observations of each star and analyzes the variation in inferred magnitude as a function of stellar color and PWV.

3.1. *A Clean Sample of Zero Points*

We define a "clean" sample of zero points as being only from the 2016A, 2017A, and 2017B semesters. We further restrict the clean sample to have zero points between 25.75–26.75 mag. The minimum cut eliminates the extended tails of lower values of zero points from images taken in higher-opacity conditions, while the maximum cut eliminates a few outliers at greater than 26.75 mag that are clearly anomalous.

The clean sample shows a normalized median absolute deviation (NMAD)[2] of 131 mmag.

---

[2] NMAD is normalized such that a Guassian distribution with a $\sigma = 1$ will have a NMAD= 1.

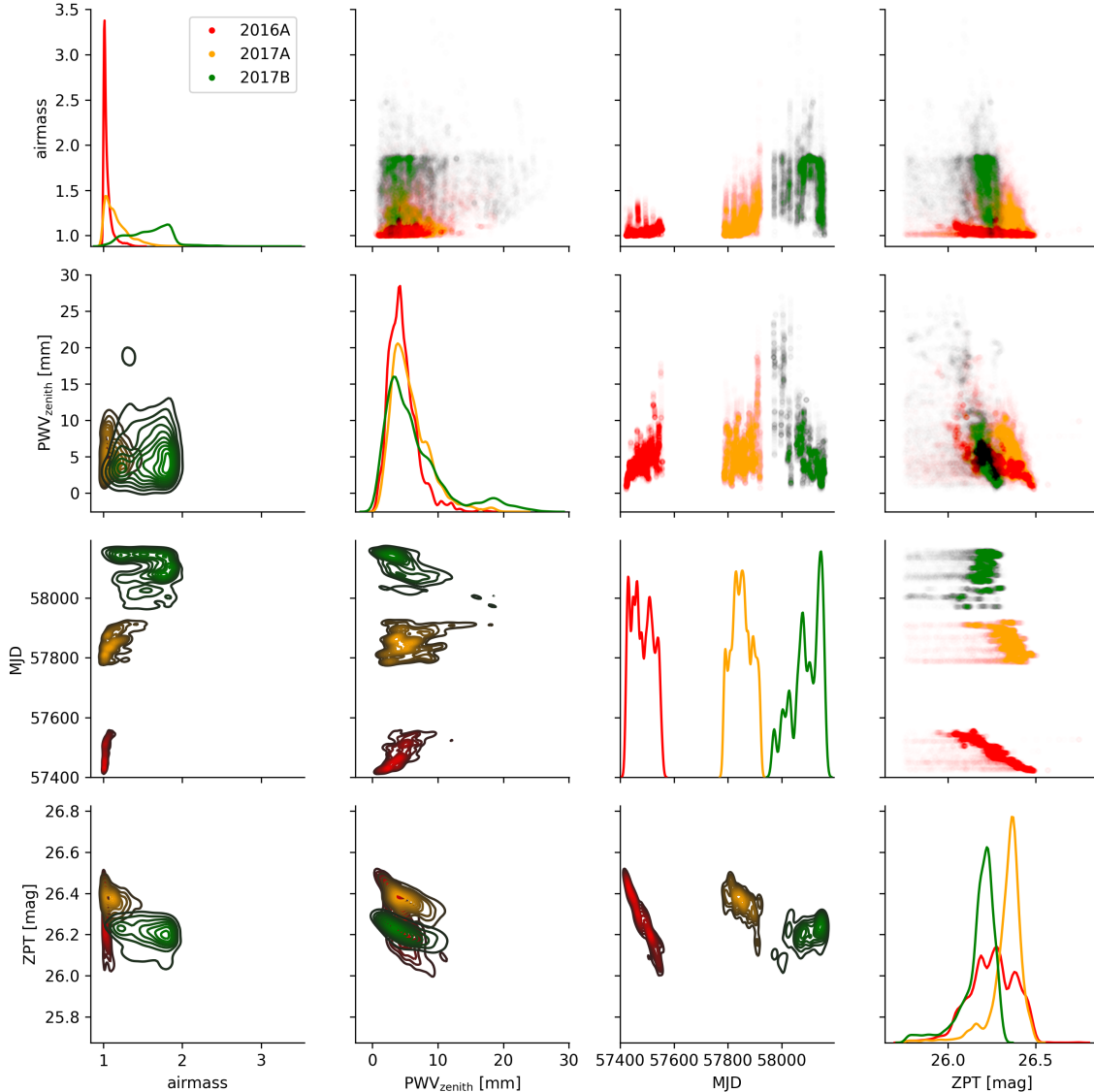**Figure 3.** The airmass, PWV_{zenith}, MJD, and zero point distribution for the MzLS data. The points and lines are color-coded by season: (red) 2016A, (yellow) 2017A, (green) 2017B. The upper-right are scatter plots, while the lower-left are contours from gaussian kernel density estimates. The diagonal plots are normalized gaussian kernel density estimates of that intersecting parameter. Note that the airmass distribution in the last semester of the survey was much wider. The distribution of PWV_{zenith} was relatively the same across seasons, but the significantly higher airmass in 2017B means that PWV_{los} was systematically greater for observations in this season.

3.2. *Image Zero Points vs. MJD*

The most immediately apparent correlation of the MzLS image zero points is a secular trend with MJD. Figure 4 shows the distribution of image zero point to MJD. This trend appears to reset on an annual basis. We first speculated that this was due to an accumulation of contaminants ("dust") on the Mayall 4-m optical surfaces. Burke et al. (2018, Fig. 9) find a similar linear decrease in sensitivity for the CTIO Blanco 4-m and DECam during the Dark Energy Survey; periodic washings restored

the sensitivity. However, when we compared to the Mayall CO_2 cleaning schedule, Fig 4, we did not find a clear correlation with the cleaning schedule. There was a potential improvement in sensitivity when the main mirror was hand washed, but the change was much smaller than the decrease over a season.

We do not have an explanation for why the slope of the decrease in ZPT with time is steeper in 2016 than in 2017. We speculate that different amounts of dust in the air or differences in air flow across optical elements may explain the difference. However, the effect is clear, on a longer time scale than PWV variations, and we can model it.

We estimate a simple linear model for a decrease in sensitivity with time. The model assumes that sensitivity is reset at the beginning of 2016A and 2017A:

$$zp = zp_{ideal} - \alpha \text{ phase} \tag{1}$$

with $zp_{ideal} = (26.50, 26.51)$ mag and $\alpha = (2.320, 0.524)$ mmag/day. The phase is defined with respect the beginning of the observing years: (2016A: 57419, 2017A+2017B: 57785) Accounting for this linear secular evolution results in an NMAD of corrected zero points of 58.6 mmag.

3.3. Image Zero Points vs. PWV

After correcting for the secular component of zero-point variation, the remaining variation in the zero points is well-explained by the variation in PWV (Figure 7). The GPS-based PWV measurement is for the PWV at zenith, PWV_{zenith}, as the combination of measurements of delays from several satellites spread across the sky with local meteorological data (pressure, temperature, humidity). Any given observation with the Mayall 4-m at an angle away from zenith will look through more water vapor. If we assume that the PWV is distributed as a uniform slab in the atmosphere, then the amount of water vapor along a given line of sight, PWV_{los}, will scale with the airmass, $X = \sec(\text{zenith angle})$,

$$PWV_{los} = PWV_{zenith} X \tag{2}$$

However, the absorption does not scale linearly with the amount of water vapor. Water vapor absorption is a rich mix of lines, many of them at relatively high optical depth even at just a few mm of PWV. Thus the water vapor absorption displays a non-linear relationship between total absorption in a given wavelength window and PWV column depth. Once an individual line saturates, increasing water vapor column depth no longer leads to additional absorption, so absorption increases with increasing PWV more slowly than linearly. Wade & Horne (1988) estimated that one could account for this saturation by calculating an effective line-of-sight PWV by scaling by airmass to the $\delta = 0.6$ power:

$$PWV_{Wade} = PWV_{zenith} X^{0.6} \tag{3}$$

This correction allows for a single linear coefficient to describe the increase in absorption (decrease in zero point, zp) with airmass:

$$zp = zp_{ideal} - \beta \ PWV_{zenith} X^{\delta} \tag{4}$$

We find that for an $\delta = 0.6$, $\beta = 12.1$ mmag/mm provides an improved fit for translating the measured zero points to a idealized constant zero point.
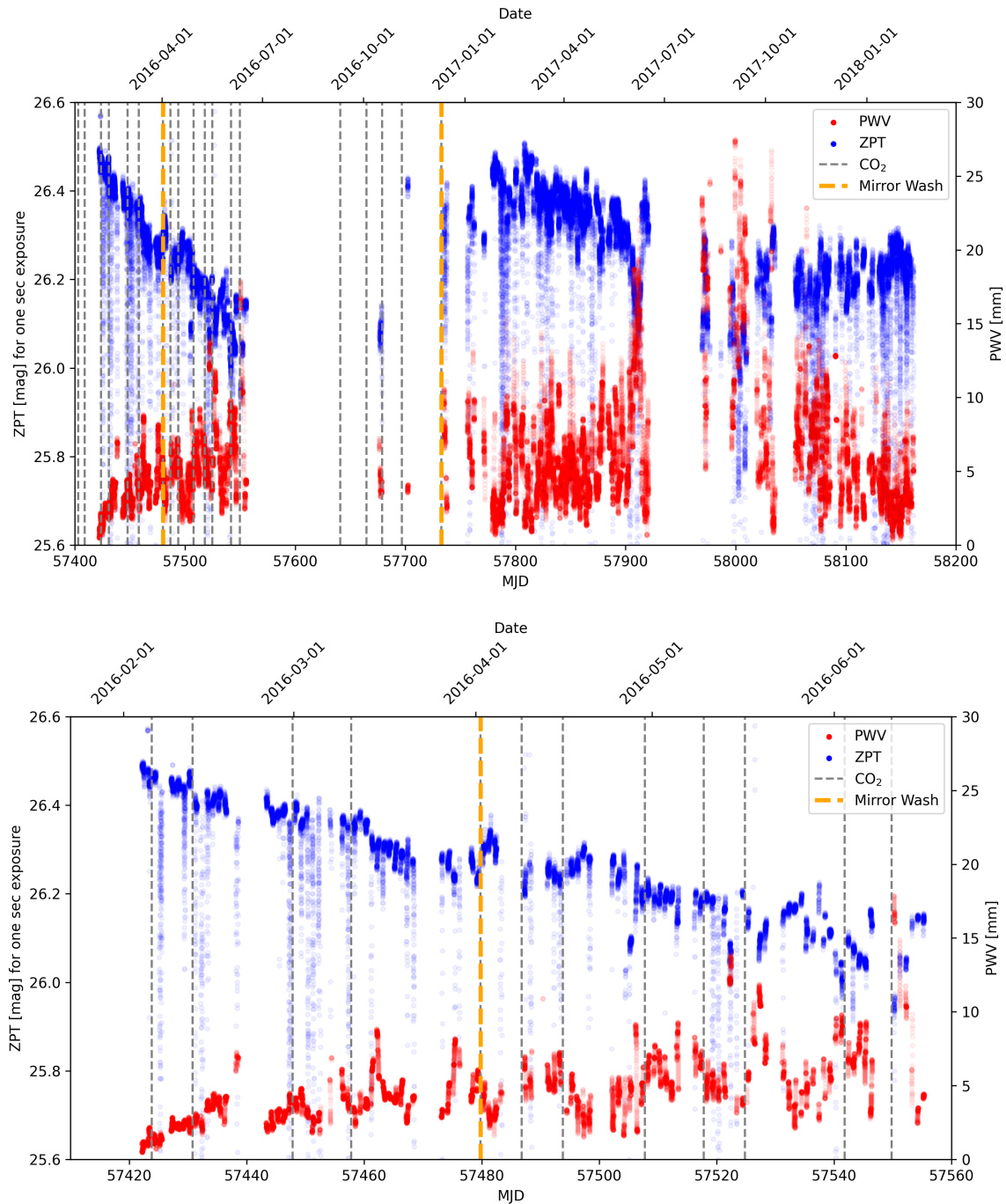
Figure 4. (top) The MzLS image zero points (blue) show a clear secular trend with time. There is also a clear anti-correlation between the zero point and the GPS-measured amount of PWV (red), but that accounts for less of the variation than the secular time evolution. However, note the very clear decreases in sensitivity associated with the very high PWV levels at MJD∼57910 and 57980–58020. The cleanings of the Mayall optics (CO_2, gray dashed) and mirror washes (gold, dash-dot) compared with the zero point and PWV measurements. There is no clear association with the CO_2 washes. (bottom) Expanded view of the first season (2016A). The full mirror wash potentially lead to an improvement in sensitivity on MJD=57480, but not nearly significant enough to return the zero point at the beginning of the season.
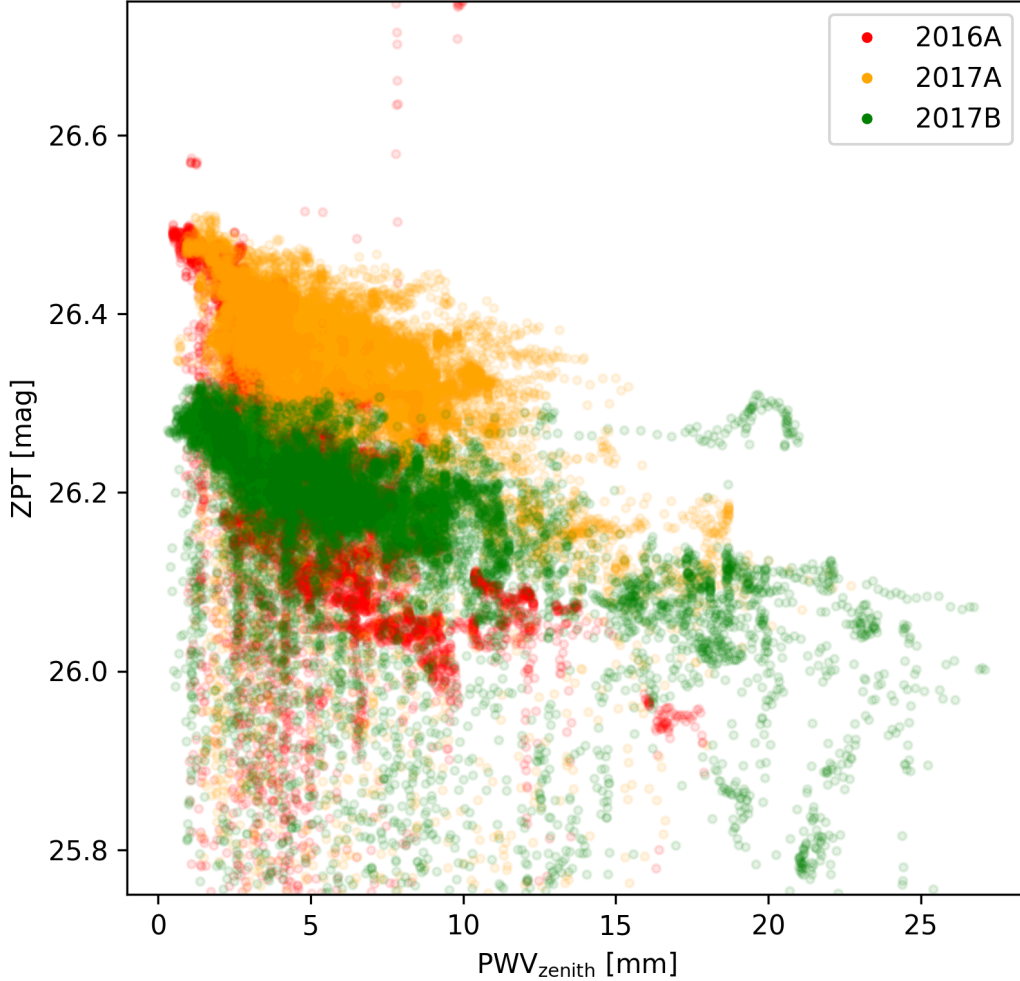
Figure 5. (left) The zero-point sensitivity for the ∼43,373 "clean" z-band exposures in the MzLS survey. The color coding gives the MJD: briefly, red is 2016A, green is 2017A, yellow is 2017B. These zero points are normalized to a one-second exposure and are *not* corrected for the MJD secular trend visible in Figure 4.

While Wade & Horne (1988) gave the scaling as just in airmass $X^{0.6}$, physically the saturation effect should follow total water vapor along the line of sight, PWV_{los}; i.e., looking through 10 mm of water vapor should yield the same absorption profile whether that's at PWV =10 mm at an airmass of 1 or PWV =5 mm at an airmass of 2. We set the normalization $PWV_{norm} = 2$ mm at the lowest value of PWV regularly measured in the data and model the zero point as

$$ zp = zp_{ideal} - \beta \ \left(\frac{PWV_{zenith}}{PWV_{norm}}X\right)^{\delta} \tag{5} $$

For this definition of effective PWV, we find $\delta = 0.6$ makes the zero-point dependence largely linear with $\beta = 31.9$ mmag/mm$^{0.6}$. This corrected effective PWV prescription corrects the zero point variation better than the Wade prescription (see Table 2).
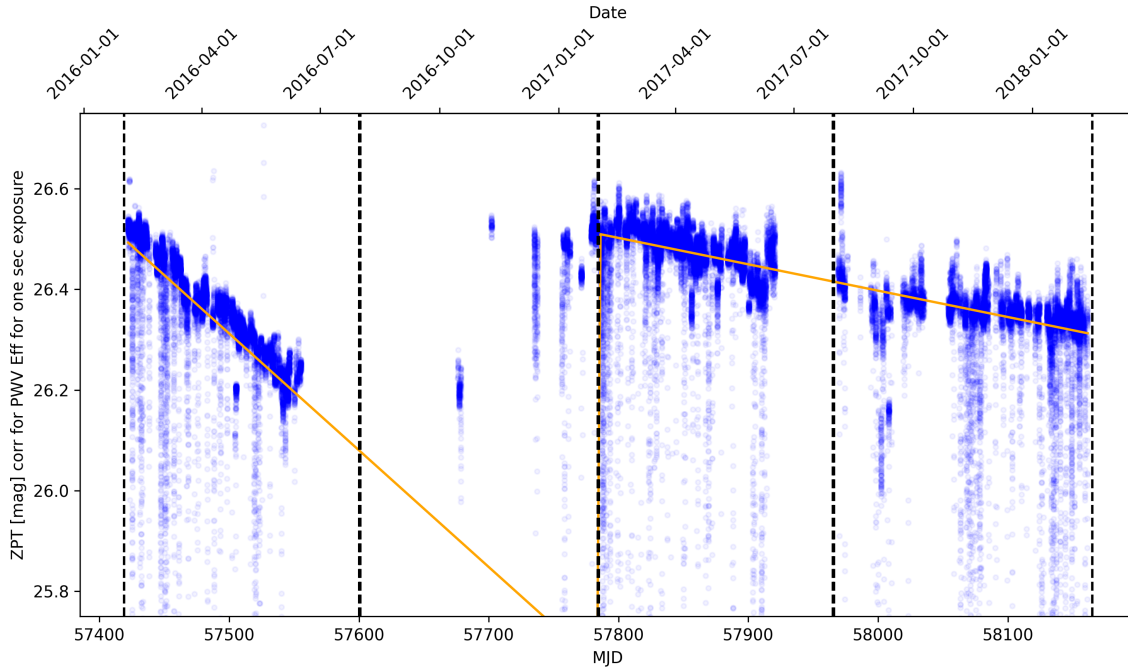
Figure 6. (blue) PWV-corrected MzLS zero point vs. MJD. If we remove the estimated effect of PWV, we get an even cleaner signal of the secular evolution of MzLS sensitivity with MJD. Note, in particular that the continuation of the trend in 2017A is now clearer in 2017B. In Figure 4 the 2017B semester appeared to flatten out from the simple linear trend of 2017A. But 2017B was a drier semester than 2017A and thus there was less absorption due to PWV and the zero points are higher. Once the difference in PWV is taken into account, the linear dependence on ZPT with MJD is more clear. (orange) Linear time evolution models per year: -2.320 mmag/day in 2016: -0.524 mmag/day in 2017. We attribute this secular time evolution to an accumulation of contaminants on optical surfaces in the telescope. Note that during the highest PWV events, e.g., MJD∼58010, the zero point loss of sensitivity is not fully explained by PWV. We hypothesize that high PWV is also associated with increased gray absorption from condensed water vapor.

Using detailed water absorption and stellar spectral models, we can directly calculate the expected absorption of a given spectral energy distribution (SED) due to a given amount of water vapor along the line of sight. Any observation contains stars of many different stellar types and the calibration will represent an aggregation across the range of stars. The full details of the calibration process depend on choice of signal-to-noise weighting and the brightness-color distribution of objects, but we here illustrate the effect by using a single representative stellar type. For the MzLS data we find that K9 star can represent the typical calibration and variation. If we are calibrating the zero point using a K9-type star, then

$$\mathrm{zp} = \mathrm{zp}_{\mathrm{ideal}} - \gamma \ \mathrm{K9}_{\mathrm{absorption}} \left(\mathrm{PWV}_{\mathrm{los}} \right) \tag{6}$$

where $\mathrm{K9}_{\mathrm{absorption}}(\mathrm{PWV}_{\mathrm{los}})$ is the predicted absorption of a K9 spectrum through $\mathrm{PWV}_{\mathrm{los}}$ as integrated over the relevant passband for which zp is being determined. If we are correctly modeling all of the relevant physics, γ should be equal to 1.

If we use this prediction for a K9 star to model the zero point variation for the MzLS data and fit for γ in Equation 6, we find $\gamma = 1.097 \pm 0.008$. While this linear fit value is formally well-constrained, a value of $\gamma = 1$ yields very similar NMAD of the residuals (29.6 mmag for $\gamma = 1.097$ and 30.6 mmag
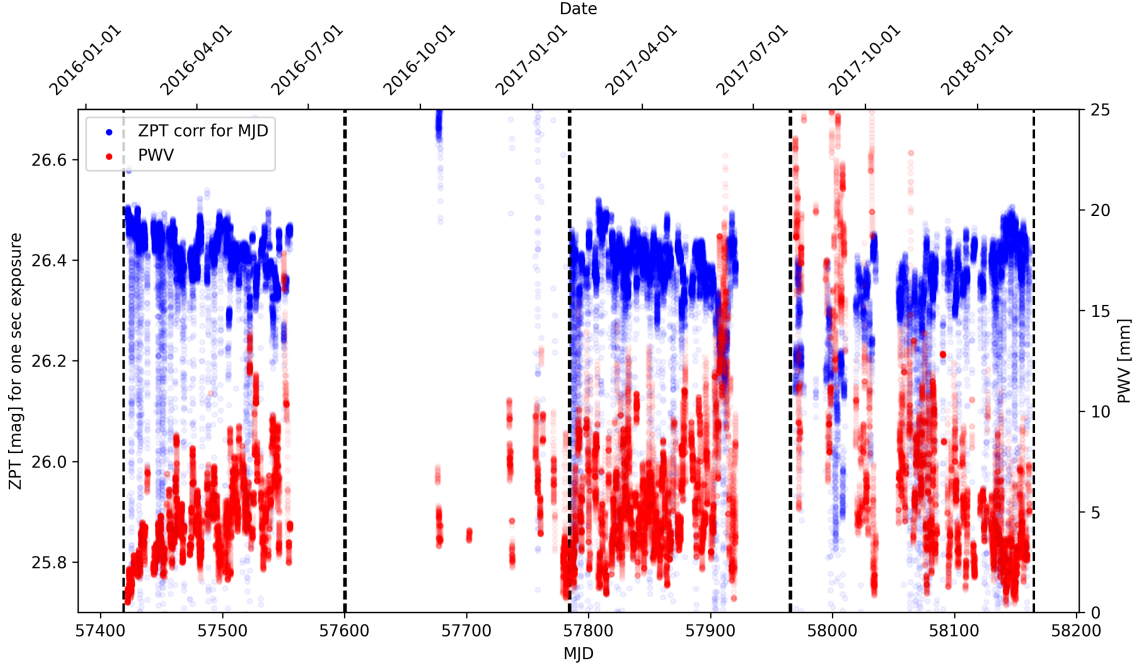
Figure 7. (blue) The MzLS zero point values corrected for secular MJD trend, but *uncorrected* for PWV. (red) The reported KPNO PWV measurements. The significant dips in MJD-corrected zero points are clearly anticorrelated with significantly elevated column densities of PWV.

for $\gamma = 1$). Because using a γ fit coefficient is not particularly well-motivated, we remove this degree of freedom (by fixing $\gamma = 1$) for the stellar+PWV model corrections used in the rest of this paper. Figure 8 compares of the distribution of the residuals after fitting with each of Equations 4, 5, and 6 (with $\gamma = 1$).

3.4. *Image Zero Points vs. (MJD, PWV)*

The previous sections presented an iterative fit with zpt_{mjd} first calculated based on the zero point corrected by the fit dependency on MJD, and then fit for γ. We here jointly fit for a per-season MJD dependence and a PWV dependence. Due to the paucity of the data in 2016B, we ignore data from that semester.

We find that the zero points are well explained by the K9 model, which is a model that is directly physically motivated by stellar spectra and PWV absorption profiles:

$$\text{zp} = \text{zp}_{\text{ideal}} - \alpha \ \text{phase} - \gamma \ \text{K9}_{\text{absorption}} \left(\text{PWV}_{\text{los}} \right) \tag{7}$$

with $\text{zp}_{\text{ideal}} = (25.3421, 26.4312, 26.3874)$ mag, $\alpha = (2.087, 0.294, 0.406)$ mmag/day, and $\gamma = (0.9963, 1.0863, 1.0968)$. The triplets of quantities refer to the seasons (2016A, 2017A, 2017B). The phase is defined with respect the beginning of the observing years: (2016A: MJD 57419, 2017A+2017B: MJD 57785). Note that the α from the PWV_{los} and $\text{PWV}_{\text{los}}^{\text{eff}}$ models are consistent.

The zero point variations can also be explained by the simple $\text{PWV}_{\text{los}}^{\text{eff}}$ model:

$$\text{zp} = \text{zp}_{\text{ideal}} - \alpha \ \text{phase} - \beta \ \text{PWV}_{\text{los}}^{\text{eff}} \tag{8}$$
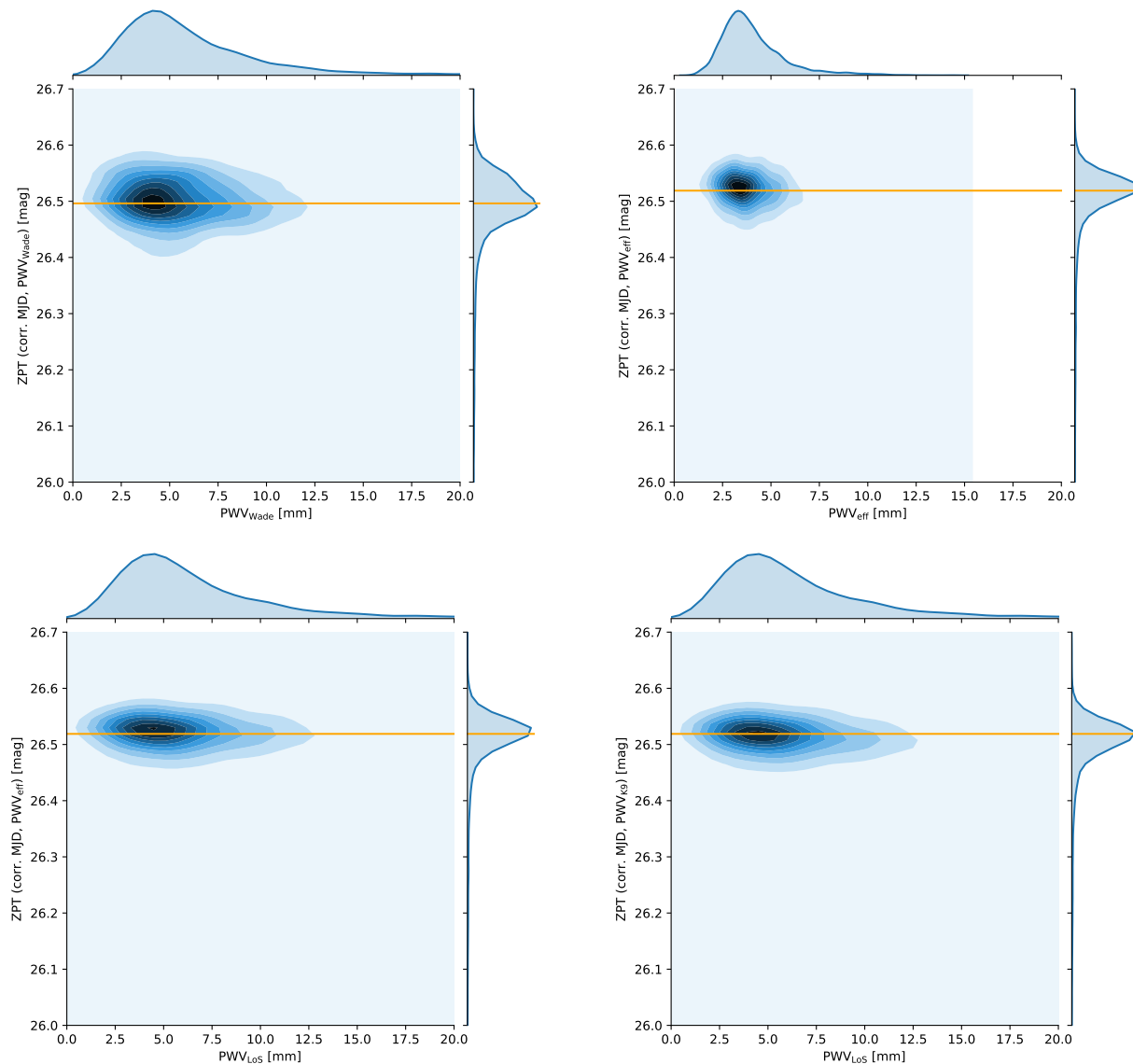
Figure 8. MzLS MJD-corrected and PWV-corrected zero point for four different methods of calculating effective PWV and correcting for it. (top left) corrected by $0.0121 \times \mathrm{PWV_{zenith}}(X)^{0.6}$; (top right) $0.0318 \times (\mathrm{PWV_{zenith}}X)^{0.6}$; (bottom left) same but plotted against $\mathrm{PWV_{los}}$; (bottom right) corrected by the absorption expected for a K9 stellar model. The orange horizontal lines are the median of each corrected zero point distribution.

with $\mathrm{zp_{ideal}} = (25.3450, 26.4330, 26.3812)$ mag, $\alpha = (2.088, 0.281, 0.415)$ mmag/day, and $\beta = (40.80, 43.12, 40.87)$ mmag/mm$^{0.6}$.

The $\mathrm{PWV_{Wade}}$ is also successful, but not as good as our $\mathrm{PWV_{los}^{eff}}$ definition. The difference is particularly noticeable in the 2017B season of MzLS. In this season the median airmass was significantly higher because the MzLS fields are not overhead at the beginning of the B semesters. But the the median PWV (after the first few weeks) was significantly lower. Thus the $\mathrm{PWV_{los}}$ distribution was similar to other semester but the $\mathrm{PWV_{Wade}}$ distribution was higher. Thus $\mathrm{PWV_{Wade}}$ the nominal zero point correction coefficient fit on a per-season basis was 14% lower between 2017A and 2017B
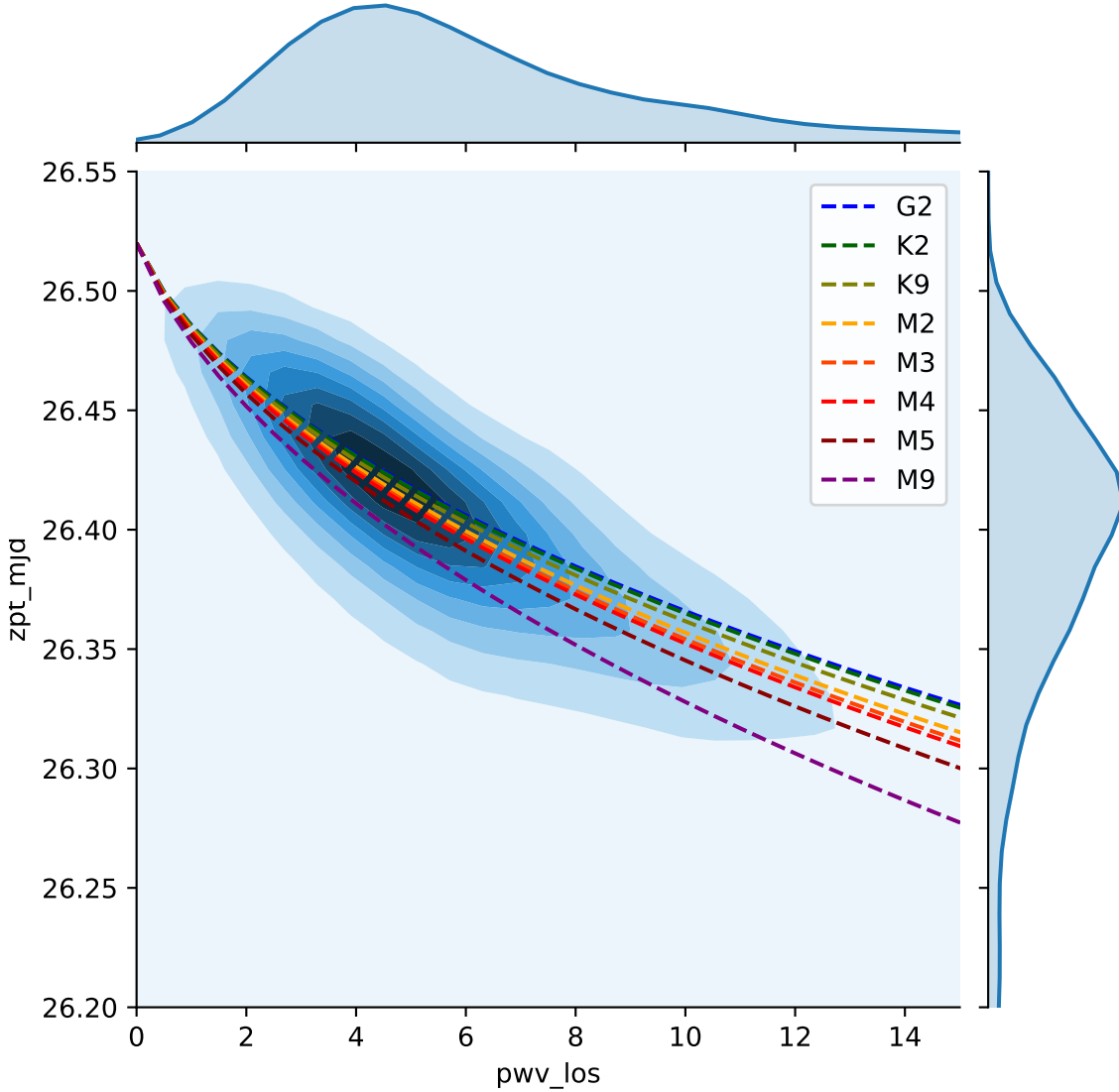
Figure 9. MzLS MJD-corrected zero point vs. PWV_{los}. Overlaid in dashed lines are the expected change in z-band transmission when observing different stellar types: G2 (blue), K2 (dark green), K9 (olive), M2 (orange), M3 (orange-red), M4 (red), M5 (dark red), and M9 (purple).

to account for this increased range of airmass at a comparable PWV_{los}, while the zero point correct coefficient was consistent for PWV_{los}^{eff} between those two semesters.

Figure 9 shows the expected zero-point offsets as a function of PWV for a different stellar types overlaid with the MzLS zero points. The calculation of these offsets is described in detail in Section 5.1. Table 2 summarizes the coefficients for the different models for zero point based on MJD and PWV.

3.5. *MzLS Per-Exposure Magnitude Deviations Depend on Color and PWV*

The DESI Legacy Survey DR8 provides per-image forced-photometry. We here explore the correlation between the per-image measured magnitude of a star, its color, and PWV.

Table 2. Zero point, MJD, PWV coefficients, NMAD

Type	Period	$\mathrm{zp_{ideal}}$ [mag]	α [mmag/day]	β [mmag/mm$^{0.4}$]	γ	NMAD [mmag]
Raw	2016–2017	$\cdots$	$\cdots$	$\cdots$	$\cdots$	130.9
MJD	(2016, 2017)	(26.50, 26.51)	(2.320, 0.524)	$\cdots$	$\cdots$	58.6
MJD + PWV$_{\mathrm{Wade}}$				12.1	$\cdots$	42.5
MJD + PWV$_{\mathrm{los}}^{\mathrm{eff}}$				31.9	$\cdots$	29.5
MJD + K9				$\cdots$	1.127	30.6
Joint (MJD, PWV$_{\mathrm{Wade}}$)	2016A	25.289	2.116	12.63	$\cdots$	31.7
	2017A	26.380	0.303	12.74	$\cdots$	33.1
	2017B	26.320	0.426	10.96	$\cdots$	33.4
Joint (MJD, PWV$_{\mathrm{los}}^{\mathrm{eff}}$)	2016A	25.345	2.088	40.80	$\cdots$	31.2
	2017A	26.433	0.281	43.12	$\cdots$	33.1
	2017B	26.381	0.415	40.87	$\cdots$	28.0
Joint (MJD, K9)	2016A	25.342	2.087	$\cdots$	0.996	31.2
	2017A	26.431	0.294	$\cdots$	1.086	33.0
	2017B	26.387	0.406	$\cdots$	1.097	27.5

NOTE—Ideal zero points and MJD and PWV model coefficients. NMAD for corrected zero point using given model. The "MJD *" rows fit per-year MJD terms first and then one overall coefficient for each PWV measurement. The "Joint *" rows are for simultaneous fitting of coefficients for both on a per-semester basis.

First, some definitions for what will be a confusing discussion of differences of differences. If z_j^i is the z-band magnitude for star i measured on image j, then we are interested in $\Delta z_j^i = z_j^i - <z^i>$, where $<z^i>$ is the average[3] magnitude based on all of the survey images. PWV$_{\mathrm{los}\ j}$ is the measured PWV$_{\mathrm{los}}$ for image j.

The stars observed by MzLS span the range of stellar types from F5–M4 stars (Figure 10). We here look at the relative change in z-band flux of specific objects under varying amounts of PWV as a function of object color. We group stars into three broad color categories: "blue": $r - z \leq 0.5$ mag; "green": 0.5 mag $< r - z \leq 1.2$ mag; "red": 1.2 mag $< r - z$. While these color ranges are only loosely motivated, they end up being illustrative. The "blue" cut is in the middle of G-type stars – the mean color of the PS1 stars used to establish the MzLS calibration is close to a K9 (see Figure 19). The "red" cut marks the beginning of the M-dwarf sequence, which is where the stellar locus goes vertical in $r - z$ vs. $g - r$. The g and r-band magnitudes are from the Bok 90" observations from the Beijing-Arizona Sky Survey (BASS)[4] component of the DESI Legacy Survey, and the z-band magnitudes are determined from the MzLS observations.

Fig. 10 shows a (median, mean) $r - z$ color for MzLS observed stars of (0.85, 0.97) mag. A K9 dwarf star has a color of $r - z = 0.93$ mag, which is right in between these values. Thus even without fully recreating the calibration of the MzLS survey, one would still reasonably expect that this typical

---

[3] It's not necessarily an average. See Legacy Survey paper for details.
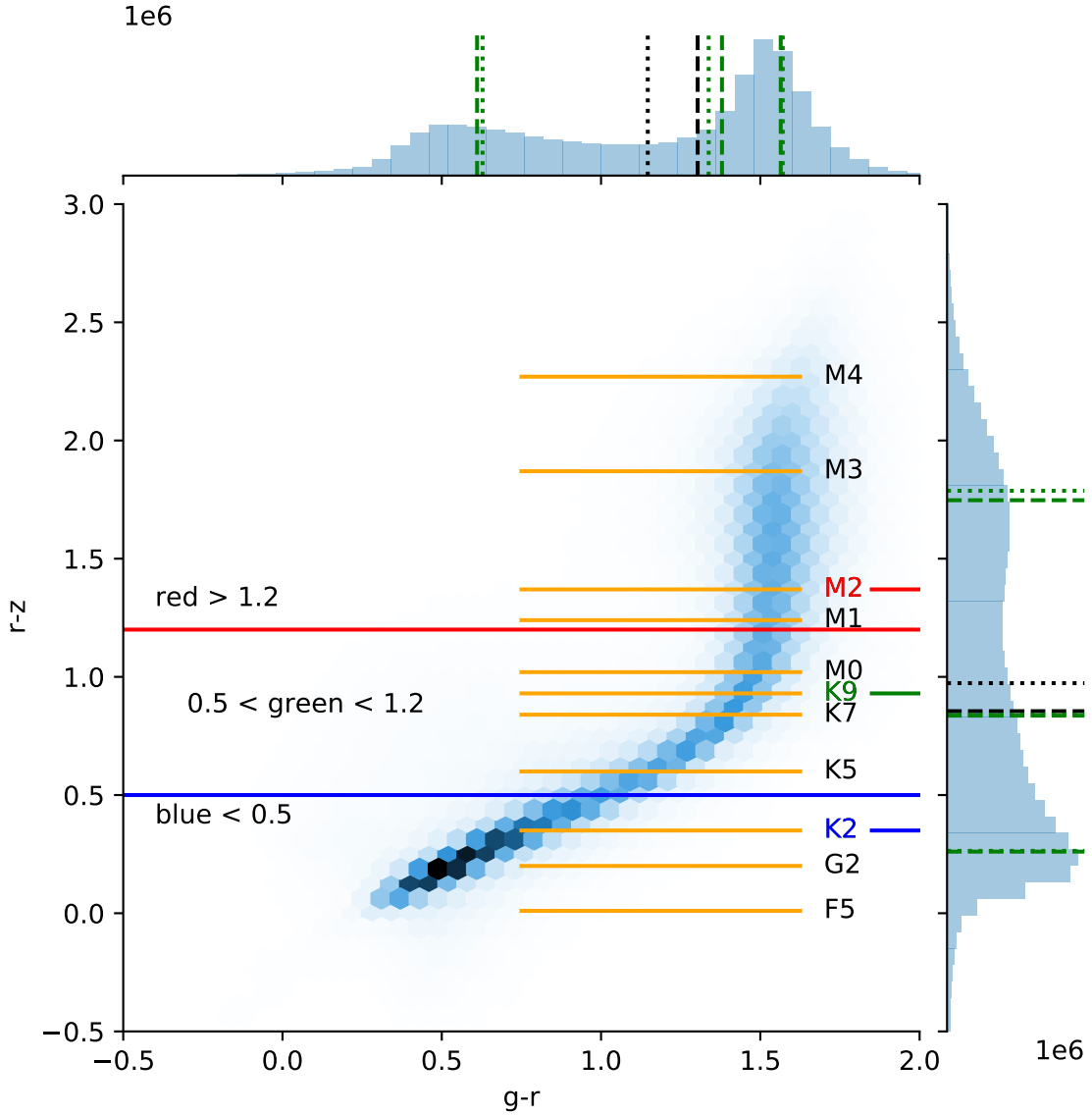
[4] http://www.legacysurvey.org/bass/

Figure 10. Stellar locus for DESI Legacy Survey stars in the MzLS footprint. No correction has been made for Milky Way extinction. The blue, green, and red $r - z$ color regions are indicated along with the nominal $r - z$ colors of a range of stellar types. The top (side) panels are the projected histograms for $g - r$ $(r - z)$. The overall median (black dashed) and mean (black dotted) colors are consistent with a K9 star. For each color region the median and mean value are very close. We have chosen representative stellar types of K2, K9, and M2. Note that while the nominal mean/median red color is notably redder than the M2 (M2.0) stellar spectrum, it is still within the range between M2 and M3.

color will remain correctly calibrated through a variety of PWV conditions. These blue−green and blue−red relations should cross through zero when the conditions match the "average" conditions of the set of data considered by the MzLS catalog calibration. At higher PWV_{los}, progressively bluer (redder) stars should be brighter (fainter).

The DESI Legacy Survey is divided into $0.25° \times 0.25°$ "bricks" on the sky. We restrict our analysis to stars in bricks that had a median of three or more exposures contributing to the pixels in the brick: "nexp_z > 3". This reduced our sample from 93,610 bricks to 81,934 bricks. We successfully

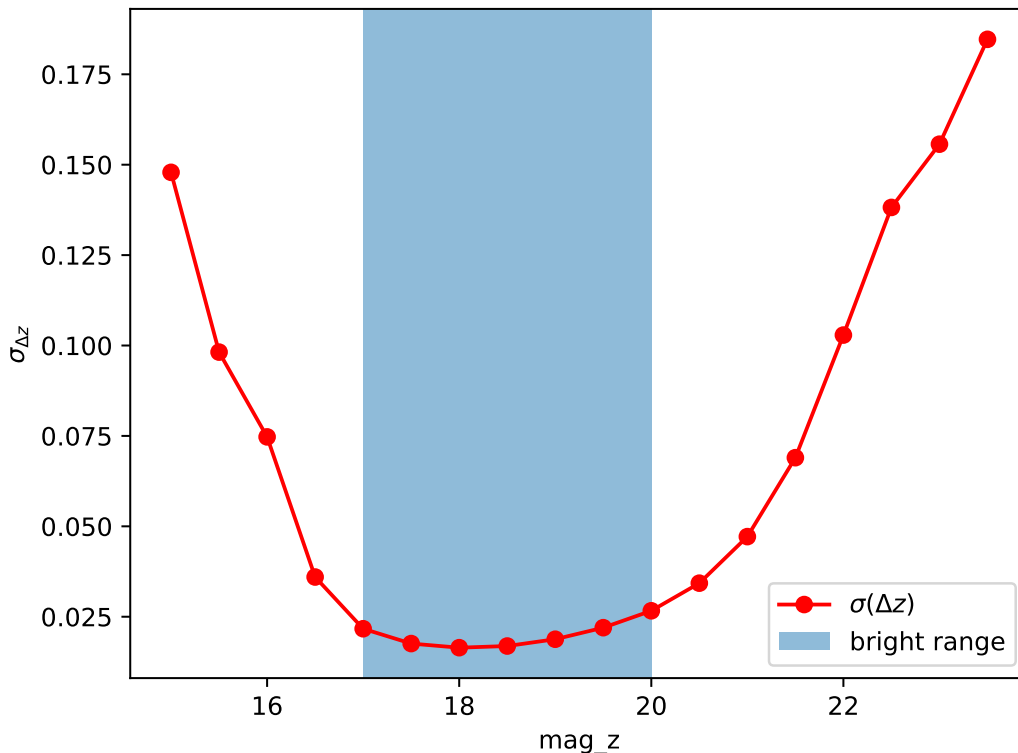**Figure 11.** Standard deviation of Δz for all stars in MzLS. (red points+line) $\sigma(\Delta z)$ binned by magnitude. At bright magnitudes, the variance increases as measurements approach the saturated/non-linear region. At the faint end, the variance increases as SNR decreases. (blue rectangle) magnitude range of the "bright" sample we focus on in our Δz vs. PWV analysis.

retrieved photometry for 81,1156 of these bricks, which had data from 15,381 MzLS exposures. The Mosaic-3 field of view is $36' \times 36'$, which means that 36 bricks fit exactly into one field of view. The alignment is not perfect, in part by construction, and so 60 bricks should be relevant for any particular image. We restrict our stellar sample to objects identified as stars and with z-band SNR > 25, 0.5 mag $< g - r < 2.5$ mag, and 0.5 mag $< r - z < 5.0$ mag.

Figure 11 shows how the variance in Δz is a function of magnitude. Non-linearity/saturation drives up variance at the brighter end while decreasing SNR and increasing non-stellar contamination drives up variance at the faint end. We thus further restrict our Δz vs. PWV analysis to stars in the range of $17 < z < 20$ mag.

For each each image, and each color class, we compute the median of the distribution of Δz_j^i values. Each image, j, then has three values: Δz_j^{blue}, $\Delta z_j^{\text{green}}$, Δz_j^{red}.

Figure 12 shows the trends of $\Delta z_j^{\text{blue,green,red}}$ vs. $\text{PWV}_{\text{los }j}$. As PWV_{los} increases, Δz_j^{blue} becomes brighter, $\Delta z_j^{\text{green}}$ is flat, and Δz_j^{red} becomes fainter. This trend as a function of stellar type is consistent with a model where SEDs that are bluer or redder than the average are mis-calibrated because an effectively gray term (the zero point in the natural system) does not properly capture the significant absorption due to PWV at the red side of the z band. If the absorption were at the blue
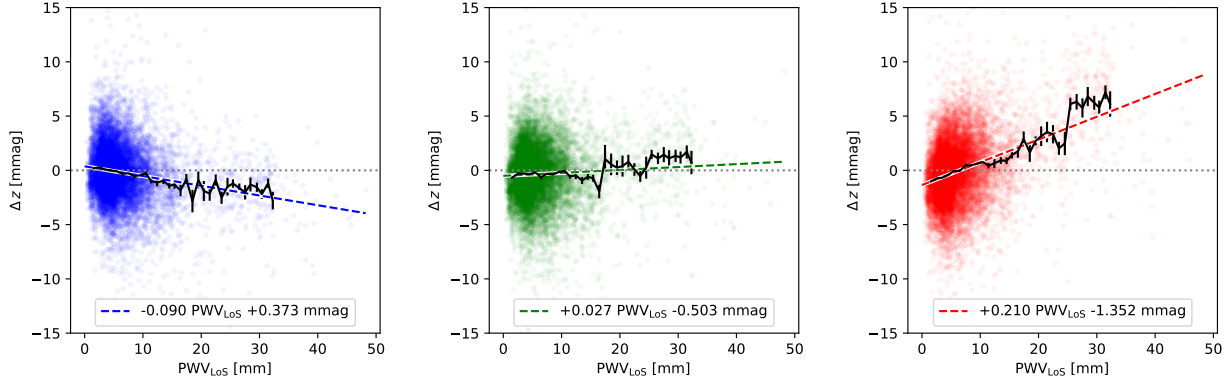
Figure 12. The per-observation variation of the z-band magnitude of stars in three color bins versus the PWV$_{\text{los}}$ for that observation. (left) blue: $r - z <0.5$ mag; (center) green: $0.5 < r - z < 1.2$ mag; (right) red: $r - z > 1.2$ mag. Each point is the median Δz for all of the stars in that color bin for that observation. The median star in MzLS has a $r - z$ a bit less than 1 mag and so the "green" panel is largely flat. The blue stars appear brighter at higher values of PWV, while the red stars are clearly fainter for high values of PWV. These binned lines intersect at the median PWV$_{\text{los}}$ of the survey: $\sim$4.83 mm.

side of the z band, then the slopes would be reversed, with blue stars being fainter at higher PWV and red stars being brighter – relative to the green stars. The flat trend in the green stars implies that they are representative of the effective average star used to calibrate the MzLS observations.

They are thus flat in Δz vs. PWV$_{\text{los}}$. For PWV$_{\text{los}}$ less than this value, the red stars are systematically brighter than their average. For PWV$_{\text{los}}$ greater than this value, the blue (red) stars are systematically brighter (fainter) than their average. The three binned lines meet at $\Delta z = 0$ mag at the median PWV$_{\text{los}}$ of the survey, ~ 4.83 mm.

Comparing the relative trend makes the correlation clearer. Figure 13 clearly shows that there is a dependence of $\Delta z_j^{\text{blue}} - \Delta z_j^{\text{green,red}}$ with PWV across the full range of measured PWV values. The dependence is well explained by the detailed PWV absorption against stellar templates from Section 5.1, but also by a simple linear fit to PWV$_{\text{los}}$ with a dependency of -0.299 mmag/mm for blue$-$red, and -0.114 mmag/mm for blue$-$green. Figure 22 in Appendix B of Burke et al. (2018) compares two different DECam exposures, one at a low PWV$_{\text{zenith}}$ and one at a high PWV$_{\text{zenith}}$. They find a clear difference in the dependence of Δz across 14 bins of stellar $g - i$ color. Our Figure 12 only divides the sample into three color bins but shows 32 bins of PWV$_{\text{los}}$.

Note that $\Delta z_j^{\text{blue,green,red}}$ being 0 at the median PWV$_{\text{los}}$ of the survey is not dependent on the relative calibration of the blue, green, and red stars in the reference catalog. We are here looking at the *difference* between the per-epoch magnitude and the overall average survey magnitude of the star. We here clearly detect the slope due to PWV$_{\text{los}}$ and show that it is explained by variation in the differential PWV absorption of stellar spectral types matching the stellar colors.

We thus have a consistent picture. Our PWV model explains the zero-point variation from the MzLS survey assuming the images were calibrated against a set of stars with a nominal color of a K9 star. The color-based residuals for stars of different stellar types are then further consistent with the difference between the effect of PWV on K9 stars and each of the different stellar types. Specifically, red stars have a median magnitude offset with respect to blue stars consistent with the difference in PWV absorption between M4 stellar spectra and K9 stellar spectra.
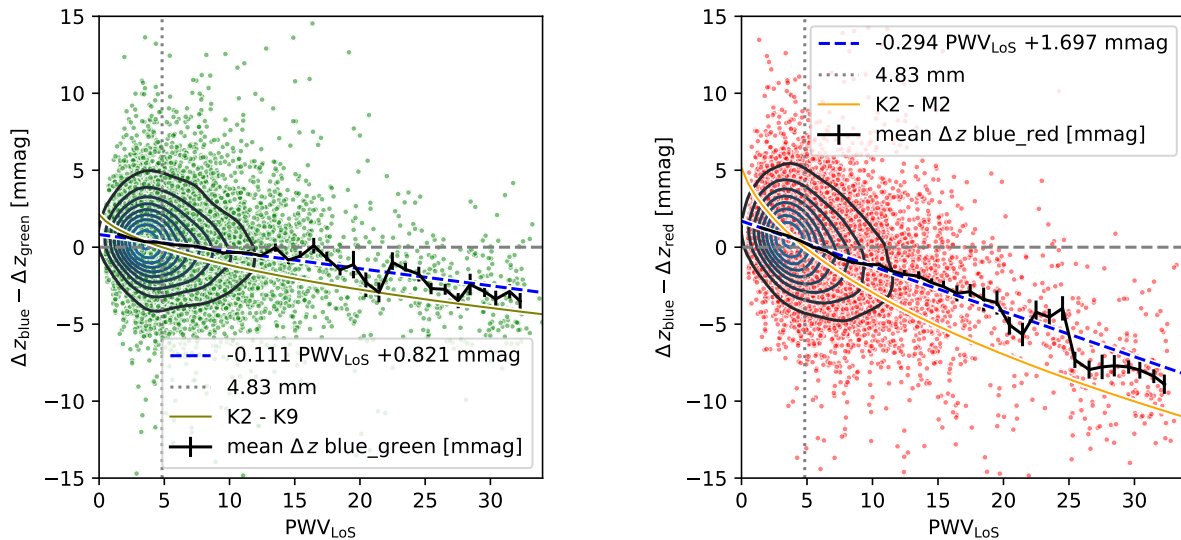
Figure 13. Difference in median Δz between different color stars versus PWV_{los} (blue points, with density estimation contours as solid lines). (left) blue−green: These are blue points minus the green points from Figure 12. (right) blue−red: These are blue points minus the red points from Figure 12. This correlation is reasonably explained by the variation of the calibrated brightness of a M4 star calibrated with a K9 star (orange solid line) through different PWV_{los} as shown in Figure 18. This model has been set to 0 at the median PWV_{los} value of 4.83 mm. The correlations for each color difference are reasonably explained by a simple linear fit (green dashed line), which reinforces the utility of using PWV_{los} as a practical quantity to understand the effect of PWV on absorption. Note that because this is the $\Delta z_{blue} - \Delta z_{red}$, negative values here mean that the inferred magnitudes of red stars are fainter than those of blue stars compared to their average magnitudes. Thus negative values are consistent with increased absorption due to PWV. This is the same convention as in Figure 18.

Figure 14 shows the dependence of median blue $\Delta z-$ median red Δz vs. MJD. Because there's little correlation between MJD and PWV on these scales, the distribution should not be expected to show any clear trends. The deviations are still there, they've just been scrambled up by looking at MJD instead of PWV_{los}. The notable exception is the deviation between MJD 57950–58010. This was a particularly high PWV period and stands out in both PWV and MJD (see Figure). The median blue $\Delta z-$ median red Δz provides a separate indication that the zero-point variation had a strong color term during these nights.

We thus have a consistent picture. Our PWV model explains the zero-point variation from the MzLS survey assuming the images were calibrated against a set of stars with a median color of a K9 star. The color-based residuals for stars of different stellar types are then further consistent with the difference between the effect of PWV on K9 stars and those different types. Specifically red stars have a median magnitude offset with respect to blue stars consistent with the difference in PWV absorption between M4 stellar spectra and K9 stellar spectra.

4. CORRECT ZPT WITH ΔZ(COLOR) VS. PWV

Section 3.5 demonstrated the variation in relative brightness of stars of different colors is correlated with PWV. We here explore whether the PWV data provide additional improvements in ZPT over just using the variation in relative brightness of the stars. The question is about the basic variation
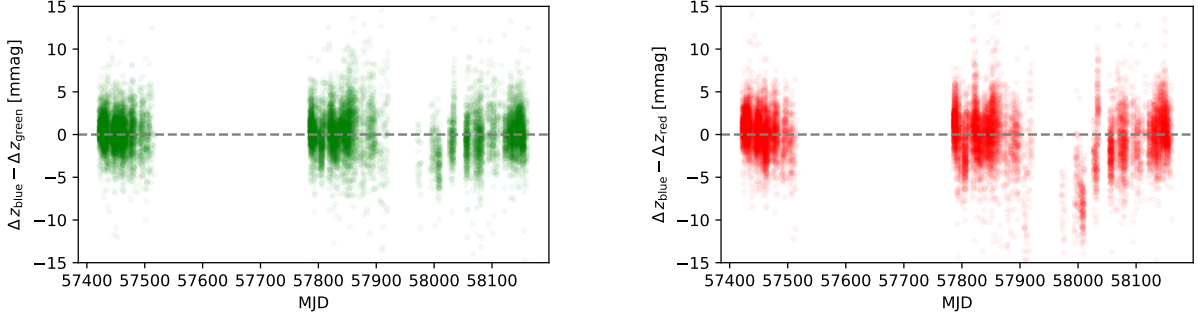
Figure 14. (left) The median blue $\Delta z-$median green Δz versus MJD. (right) The median blue $\Delta z-$median red Δz versus MJD. No correction has been made for PWV. The only clear trend is the deviation MJD=57950–58010 which is the time period with the highest PWV ($\sim$25 mm) during the survey. Note that the secular trend of MJD from Figure 6 should not be apparent in this plot as this is showing the differential measurement as a function of color.

of each measurement, the correlation with ZPT, and the outliers. An additional important question is whether the color data can supplement cases where the PWV measurements have aberrations. One could of course ask the question the other way: "can PWV help identify cases where the color-based differential brightness of stars are incorrectly calibrated?" But it would be unclear what to then do about those data. If the color-based differential brightness was systematically in error (rather than just noisy) that would imply there was something wrong in the basic extraction of flux from the image.

Figure 15 shows that $\Delta z(\text{blue} - \text{red})$ and PWV_{los} are clearly correlated, and more negative values of $\Delta z(\text{blue} - \text{red})$ and higher values of PWV_{los} are both associated with less transparent conditions (lower values of MJD-trend-corrected ZPT). However, the PWV_{los} distributions separate much more clearly with respect to MJD-trend-corrected ZPT than do the $\Delta z(\text{blue} - \text{red})$ measurements.

Figure 16 demonstrates the success of using PWV_{los} to predict MJD-trend-corrected ZPT. The expected relationship across several stellar types explains both the core of the MJD-trend-corrected ZPT variation as well as the outliers. There are a noticeable number of outliers that have lower values of MJD-trend-corrected ZPT even at low values of PWV_{los}. However, these images also have low $\Delta z(\text{blue} - \text{red})$ (refer back to Figure 15) and we hypothesize that these images have some amount of gray extinction. The residual of MJD-trend-corrected ZPT vs. the predicted stellar model dependence on PWV_{los} do not appear to be obviously correlated with $\Delta z(\text{blue} - \text{red})$.

Figure 17 shows that $\Delta z(\text{blue} - \text{red})$ is indeed correlated with MJD-trend-corrected ZPT, but is not as powerful at predicting the ZPT variation, particularly at the highest level of PWV.

We conclude that PWV_{los} is a significantly better predictor of MJD-trend-corrected ZPT than $\Delta z(\text{blue} - \text{red})$. Measurements of PWV_{los} can improve the standard deviation of the measured MJD-trend-corrected ZPT from 58 mmag to 30 mmag. Using, an admittedly simple, linear model of $\Delta z(\text{blue} - \text{red})$ to attempt to improve the MJD-trend-corrected ZPT variance results in a worse standard deviation of 69 mmag.

We end this section by mentioning two opportunities to improve the differential brightness color-based measurement of PWV: (1) survey with more repeated observations of fields in more filters; and (2) taking advantage of the temporal and spatial correlation of PWV.
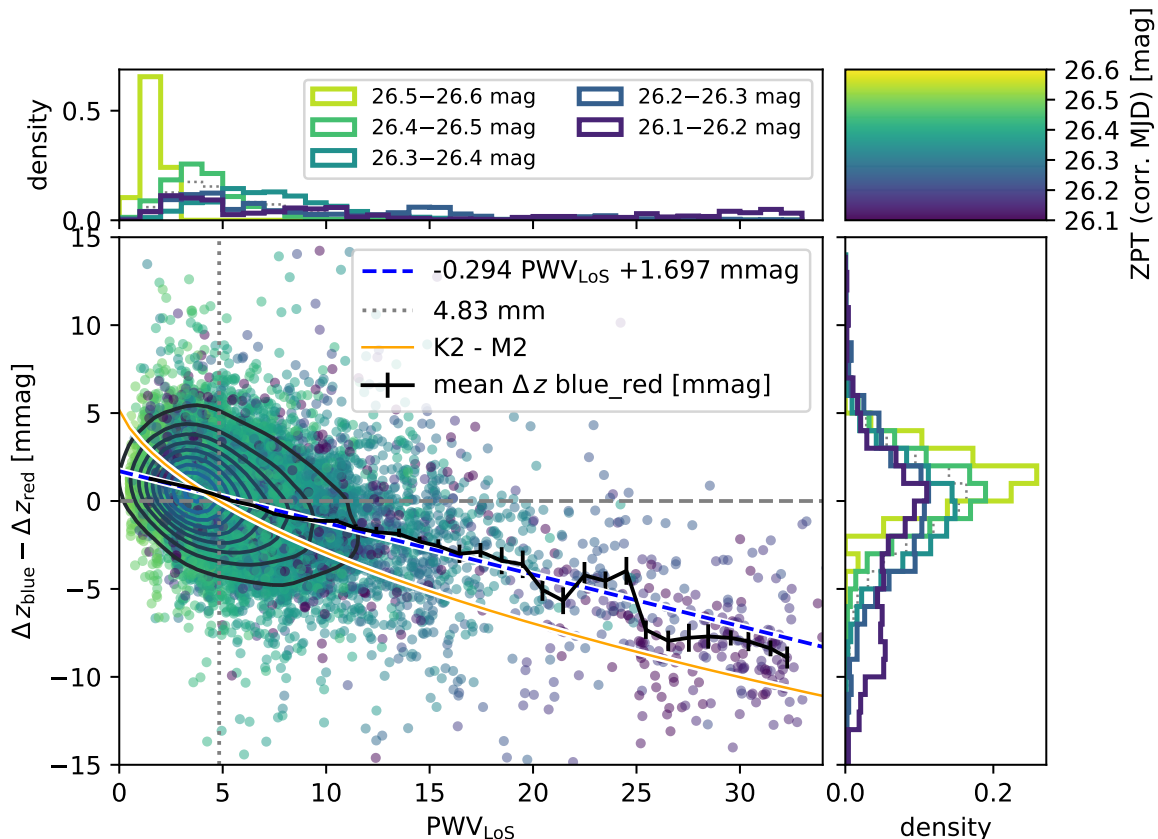
Figure 15. $\Delta z(\mathrm{blue - red})$ vs. $\mathrm{PWV_{los}}$, color-coded by ZPT corrected for MJD trend. The trend in $\Delta z(\mathrm{blue - red})$ vs. $\mathrm{PWV_{los}}$ is approximately linear in both the mean binned values (black line with errobars) and a simple linear fit (blue dashed line). A model based on the expected difference in the relative brightness of a M2−K2 star qualitatively agrees with the trend (orange line). The top (side) panels give the projected distributions of $\mathrm{PWV_{los}}$ ($\Delta z(\mathrm{blue - red})$) for different values of the MJD-trend-corrected ZPT. The $\mathrm{PWV_{los}}$ measurements separately much more clearly than the $\Delta z(\mathrm{blue - red})$ measurements. Note that the highest measured values of $\mathrm{PWV_{los}}$ consistently result in outlier ZPT measurements.

MzLS was a survey conducted in a single band with a typical limit of only three repeated observations of a star. It's possible that results for color-dependent Δz could potentially be improved in surveys that have more repeated observations over different conditions of the same field, or taking several images in different filters within an ∼hour to capture more directly the effects of PWV versus gray extinction. The gray extinction variation can be dominant over the effect of PWV. Thus measuring the gray extinction separately might allow for a cleaner differential brightness color-based measurement of the effect of PWV.

Greater power may come from including the strong temporal and spatial correlation of PWV. The model of a uniform slab across the sky varying on 30–60 minute time scales is remarkably good. It's possible that assuming some time constant for variation of PWV would allow the combination of measurements across a set of images to improve the sensitivity of using the differential brightness color-based method to correctly predict the true transmission spectrum.
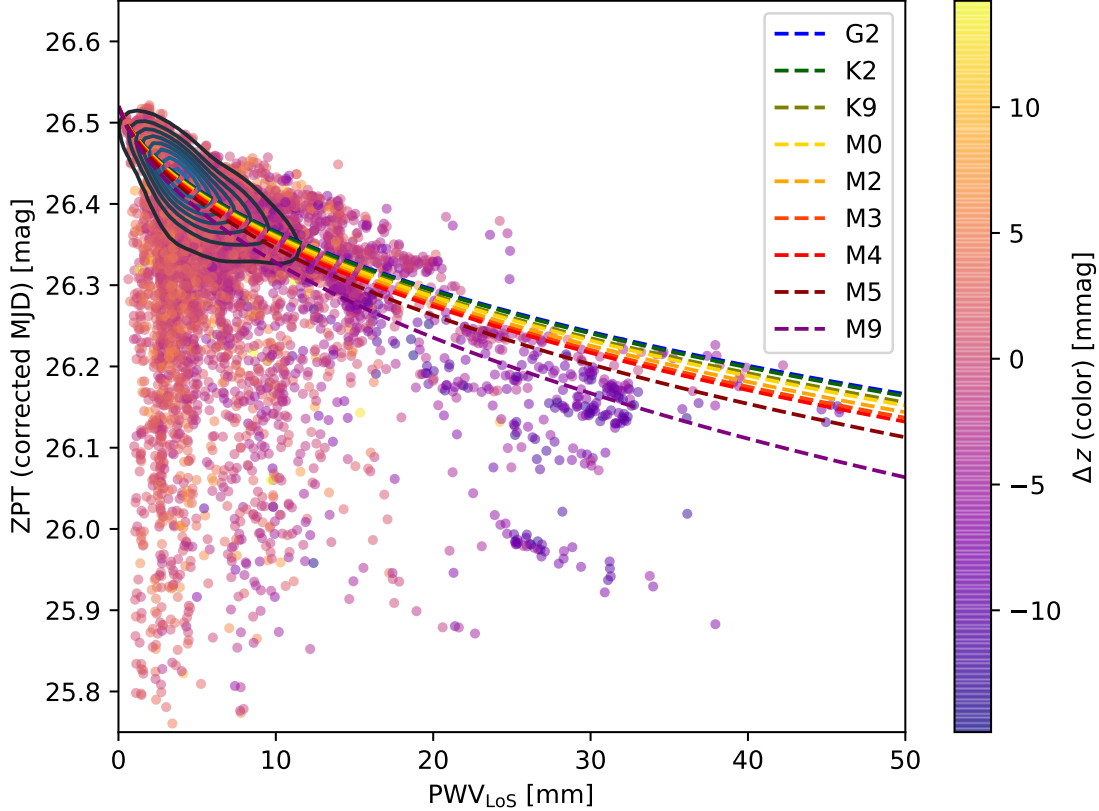
5. IMPACT ON SELECTED SCIENCE CASES

Figure 16. MzLS zero point, corrected for MJD trends, versus $\mathrm{PWV_{los}}$, and color-coded by $\Delta z(\mathrm{blue-red})$. Overlaid are the predicted effect of $\mathrm{PWV_{los}}$ on six stellar templates: G2 (blue dashed line), K2 (forest green dashed line), K9 (olive dashed line), M2 (orange dashed line), M4 (red dashed line), M9 (purple dashed line). The points with the largest $\mathrm{PWV_{los}}$ have clearly reduced z-band sensitivity and are also significantly negative in $\Delta z(\mathrm{blue-red})$. While there is visible population of zero-point variation that is not explained by PWV, these also exhibit small excursions in $\Delta z(\mathrm{color})$. We thus attribute these to gray extinction variation. Also note that while those outliers are very visible in the scatter plot, they are in fact a small fraction of the overall population, as indicated by the contour lines of the overall distribution.

We have established that PWV explains the non-secular zero-point variation of the MzLS survey and that there is a color-dependent effect for the inferred magnitudes of stars of different colors and spectral types. We next explore the consequences for PWV absorption for a wider variety of objects. We calculate the expected induced photometric error for a variety of object SEDs grouped into stars, supernova, and quasars.

5.1. *Stars*

Achieving both accuracy and precision in ground-based stellar photometry requires a full understanding of the system transmission function, including the variable atmosphere. In particular, objects whose SEDs differ from the reference catalog stars are affected differently by variable PWV absorption. Color terms can handle smooth differences in SEDs, which is particularly effective when looking at the Rayleigh-Jeans tail of stars. However, cooler stars, particularly M, L, and T stars (a) peak in emission at NIR wavelengths; and (b) have very non-blackbody SEDs with complex molecular
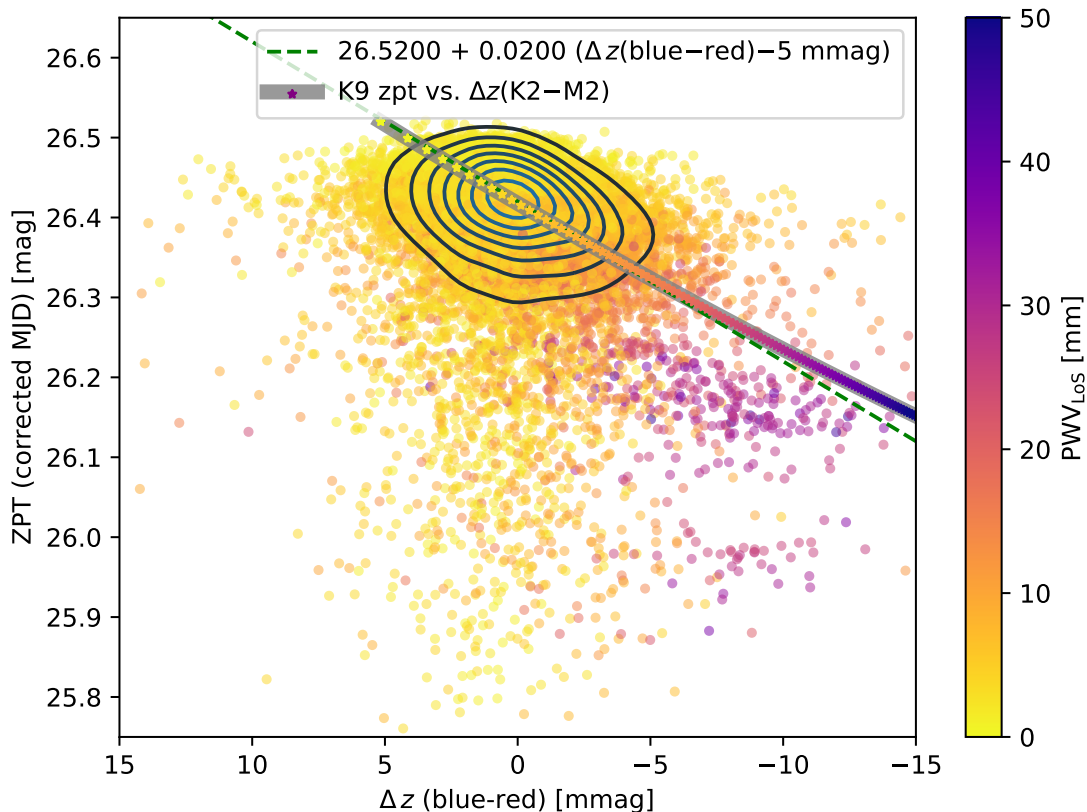
Figure 17. MzLS zero point, corrected for MJD trends, versus $\Delta z(\text{blue} - \text{red})$, color-coded by PWV_{los}. (green dashed line) A simple linear relationship explains the major axis of the contours. (grey line + stars color-coded by PWV_{los}) A model of the expected zero point change for a calibration based on a K9 star versus the expected change in relative apparent brightness between K2$-$M2 star. The model curves up from the linear model as more water lines saturate – the M2 SED remains more sensitive to the increased PWV than the K2 or K9 SEDs. While the observed zero point is in agreement with the stellar model (project the model PWV colors and the data colors onto the zero point axis), the observed $\Delta z(\text{blue} - \text{red})$ data don't go as negative as expected by the model.

band features. The impact of second order telluric absorption effects interferes with achieving precise photometry for exoplanet transit searches (e.g., Baker et al. 2017). Accurate colors are additionally important for reliable object classification.

To demonstrate the effect that PWV absorption has on stellar photometry, we integrate PHOENIX models (Husser et al. 2013) multiplied by a TAPAS water vapor transmission spectrum scaled to different PWV values. These spectra are then integrated over filter profiles to compute the flux in each band as a function of PWV. These fluxes are converted to magnitudes in each band, m, referenced to a PWV of 0 mm such that $\Delta m = m(\text{PWV}) - \text{m}(\text{PWV} = 0)$. In Figure 18 we show Δm for the r, i, and z passbands in the top panels of each figure for K9, M4, and M9 spectral types.

In the MzLS catalog, the typical reference star used for calibration is a K9 dwarf (see Figure 19). A zero point estimated for these reference stars does not correctly include the effects of PWV absorption on the integrated photometry of redder stars. The bottom panels in Figure 18 show this expected zero point error by plotting the difference in the effect of PWV absorption for K9, M4, and M9 stars.
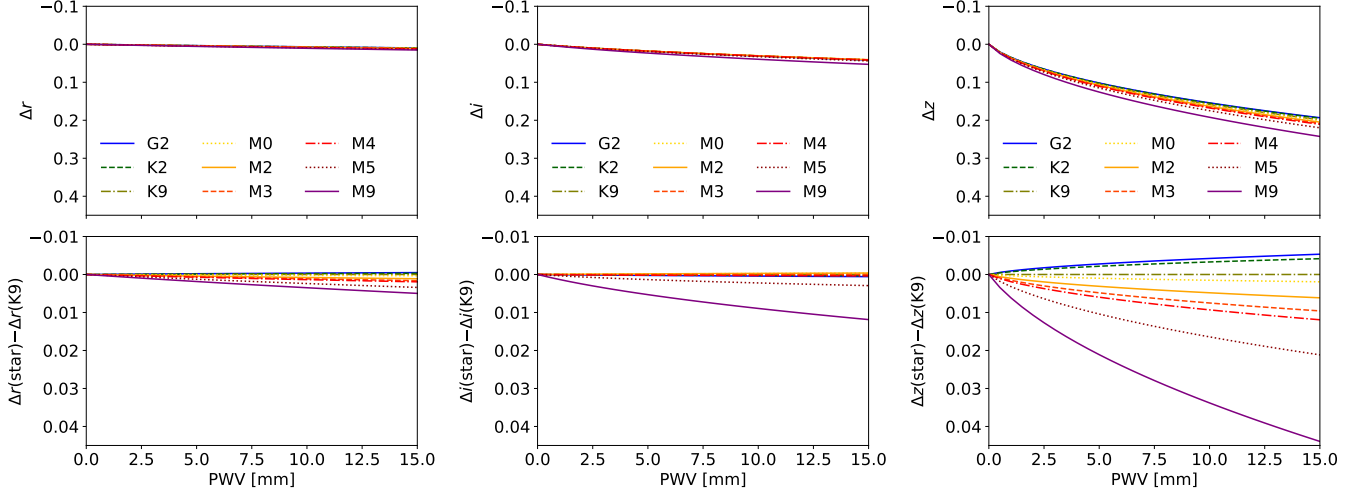
Figure 18. Change in stellar r-band (left), i-band (center), and z-band (right) photometry for G2, K2, K9, M0, M2, M3, M4, M5, and M9 stars (top) and the induced error from PWV assuming target$-$reference star combinations (bottom). The magnitude scale for the top panels is 10 times that of the bottom panels.

In nominal observing conditions (PWV = 5 mm), the error in the z-band calibrated brightness of M4 and M9 stars is 8 and 25 mmag, respectively, when calibrating with a K9 star. If instead an M4 star is used as a reference in calibration, an M9 star still has a significant brightness error of 17 mmag. This comparison shows how sensitive the effect is for stars with SEDs that vary quite substantially over a seemingly small temperature range. In the i band, the differential extinction between M4 and K9 stars is near zero whereas an M9 star would still experience a 5 mmag error. Due to the minimal amount of absorption in the r band, the error in this band is below 2 mmag for each star.

The $i - z$ color error due to these incorrect zero point corrections for an M9 star are: 15 mmag bluer at PWV_{los} =5 mm and $\sim$30 mmag bluer at PWV_{los} =10 mm. Of importance to time series data is how the magnitudes would change in time as PWV_{los} changes between observations. For this, the slopes of the curves in Figure 18 show that the z-band magnitude for M4 and M9 stars referenced to a K9 star will change approximately 2 and 5 mmag per millimeter change in PWV, respectively, in drier conditions typical of conditions at KPNO (and Cerro Pachón).

5.2. *Supernova Cosmology*

The use of Type Ia supernovae (SNe Ia) as cosmological probes relies on them having homogeneous light-curves with standardizable luminosities at the time of peak brightness. By calibrating for intrinsic variations between the absolute magnitudes of individual SNe Ia, cosmological models are used to fit SN Ia distance moduli (μ) as a function of redshift (for example, see Riess et al. 1998; Perlmutter et al. 1999; Betoule et al. 2014; Scolnic et al. 2018; Abbott et al. 2019). However, as SN Ia samples grow larger, the variation in brightness between individual SNe no longer becomes the limiting issue. Instead, common systematics that change the effective average difference for large subsets of the sample become important. Photometric calibration, and a proper treatment of PWV, are thus key in achieving the goals of large surveys such as LSST.

The importance of calibration in controlling cosmological uncertainties is well demonstrated in the literature. In the recent cosmological analysis of the Pantheon SN Ia sample (Scolnic et al. 2018), photometric calibration uncertainties contributed between 2 and 6 mmag, constituting up to
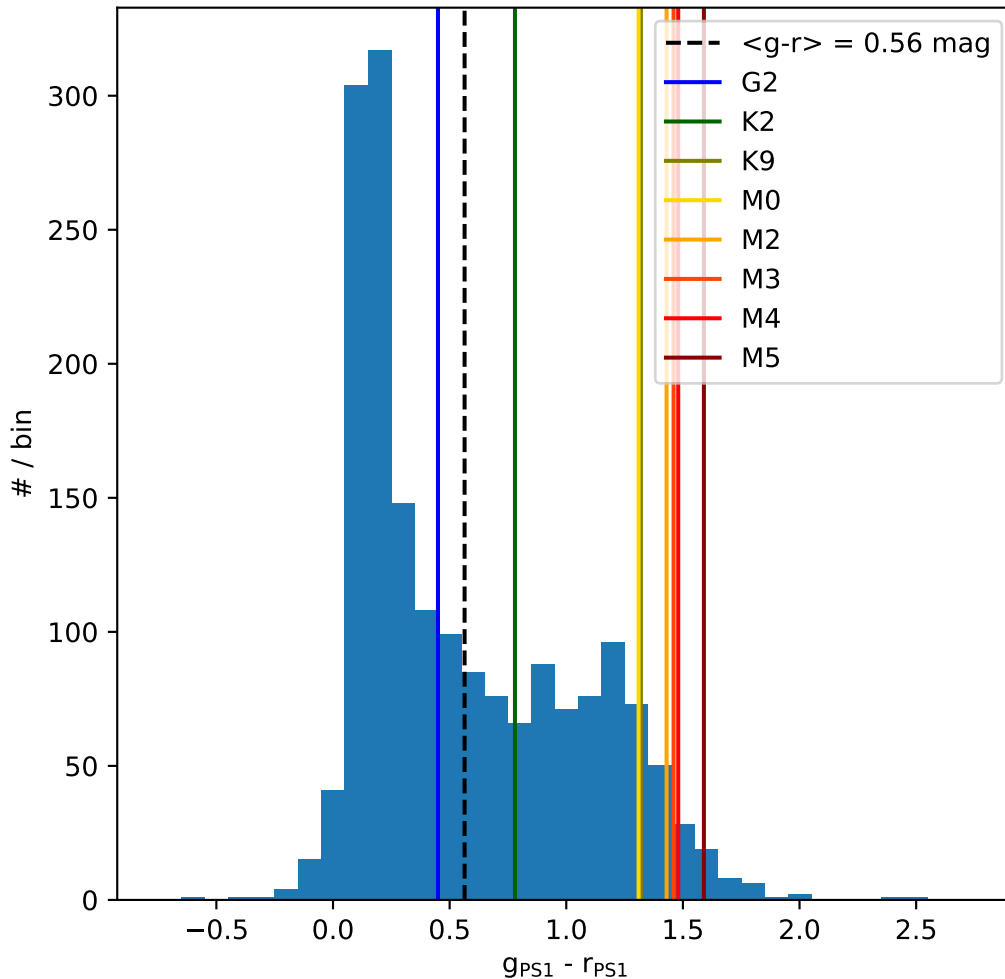
Figure 19. The $g-r$ color distribution of the PS1 reference catalog used for the MzLS calibration. Reference stars of different colors will be affected differently by varying PWV amounts. The mean color is between that of a K9 star and a K2 star. If one assumes that the calibration effectively takes an average over the mean color of the reference catalog, then the PWV effect should go approximately with the mean color of the reference stars.

half of the total uncertainty in cosmological parameters. Similarly, in Lasker et al. (2019) system transmission uncertainties introduced a redshift-dependent bias in SN Ia luminosity distances of ~ 0.02 mag. While we note in both cases that atmospheric effects were not considered separately from instrument throughput, we argue that variable atmospheric absorption can play a significant role in the z-band calibration uncertainties, particularly in thicker CCDs with increased sensitivity in the 940–980 nm water band.

The SEDs of SNe Ia are quantitatively different than stars. They have wide absorption lines characteristic of the elemental composition and 10,000 km s^{-1} typical explosion speeds. SN Ia light-curve fitting uses this and models the spectrum of SN Ia as part of the forward modeling, but it needs
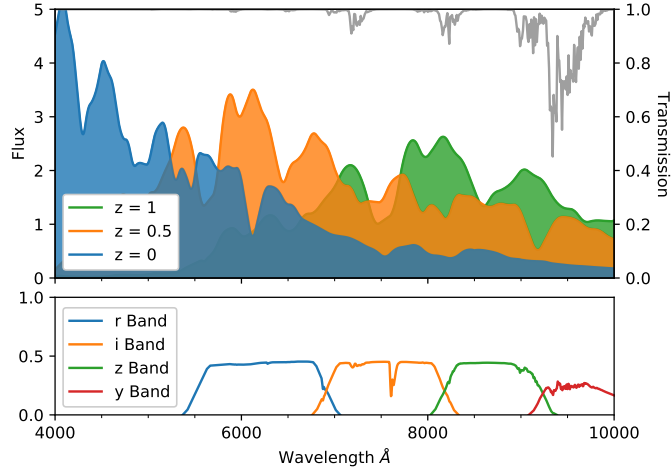
Figure 20. The spectral template of the Salt2 supernova model for a redshift of 0.1 (blue), 0.5 (orange), and 1 (green) against the PWV transmission (grey) for a PWV concentration of 4 mm. SN Ia spectra are dominated by several broad absorption features, many of which have equivalent-widths similar to the widths of PWV absorption features in the zy bands. As the template spectrum is shifted to higher redshifts, different spectral features begin to overlap with the strong PWV absorption feature at $\lambda \approx 950$ nm.

an accurate and precise transmission function to do so. Photometric calibration based on the stars in the image traditionally provides just a color term, which is the equivalent of a smooth variation of the transmission function. To precisely calibrated SNeIa, the full transmission function needs to be determined, including the highly non-smooth variation due to PWV absorption.

The complex structure of PWV absorption features is neither uniform nor constant. The variation in PWV absorption causes the apparent brightness of observed targets to vary as a function of redshift, as different features are redshifted across the water absorption bands. This effect is most significant for high-redshift SNe Ia ($z \sim 1$) when the brightest region of the SED ($\lambda \approx 400$ nm) begins to enter the z and y bands (see Figure 20). However, even for low redshift targets, temporal variations in the atmospheric transmission function introduce a bias in the estimated color of SNe Ia.

To demonstrate how PWV absorption impacts photometric SNe Ia observations, we use the SALT2 spectroscopic template from Guy et al. (2007) to simulate sets of SN Ia light-curves for a range of PWV values and over a redshift range of $0 \lesssim z \leq 1$. We assume a fixed PWV concentration for each set of SNe Ia. The simulated light-curves are then fit using the SALT2 model without a PWV component. For simplicity, we simulate SNe Ia having the fiducial model stretch ($x_1 = 1$) and color ($c = 0$). We also fix t_0 and z to the simulated values. We simulate a daily observational cadence in each of the $rizy$ bands. The supernova is thus sampled in phase from (-15 − +50)/(1+z) days. The other SALT2 model parameters, x_0, x_1 and c, are left free with flat, independent priors.

Figure 21 shows the residuals in the distance moduli as determined from the simulated SNe. Note that this makes the unphysical assumption that PWV is constant for all points in the SN Ia lightcurve. In realistic conditions, PWV would vary and these biases would be averaged down. However, a season dependence of average PWV would translate into a bias as a function of RA as there is a correlation between average PWV and observed RA. Even for relatively dry, photometric conditions (PWV $\lesssim 4$), uncorrected PWV absorption introduces a bias of up to 0.02 mag in the estimated μ. A similarly sized shift is also found for low redshift targets suffering from PWV absorption that varies by more
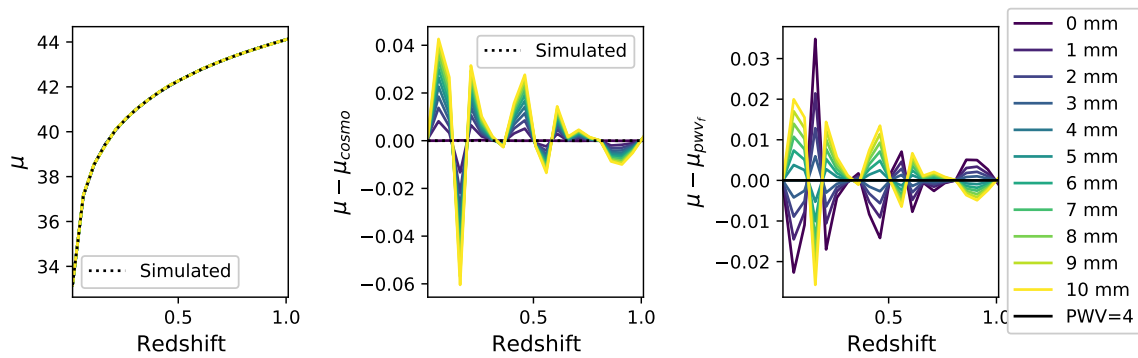
Figure 21. Distance modulus residuals ($\Delta\mu$) determined from a set of simulated SNe Ia, each suffering from a different level of PWV absorption (assumed constant for the full light curve). Residuals are shown both relative to the underlying cosmology of the simulation (center) and to a fiducial atmosphere of 4 mm PWV (right). The pattern with redshift comes from the broad features of SN Ia spectra moving across the water vapor absorption features.

than a few mm away from the assumed fiducial atmospheric value. This is just another reminder that the assumption of a fiducial transmission model that is constant from image to image, such as when constructing the effective bandpass throughputs for a given survey, is not sufficient for achieving the millimag level of precision anticipated from future large scale surveys.

We note that our results are similar in size to Hubble residuals found in existing cosmological analyses. For example, after assuming a mean atmospheric absorption model to calibrate instrumental magnitudes, the cosmological analysis of Betoule et al. (2014) found average residuals in the fitted μ of approximately 0.01 and 0.06 mag for their low and high redshift SN samples respectively. Calibration uncertainties were the largest contributing factor in measurement uncertainty, and made up over 36% of the measurement uncertainty in Ω_m.

5.3. *Quasars*

The sample of known quasars has grown substantially in last two decades thanks to surveys like SDSS, Pan-STARRS, and DES (Richards et al. 2009; Schindler et al. 2019; Tie et al. 2017). The current sample of over a million quasars is expected to grow tenfold with LSST (LSST Science Collaboration et al. 2009). With such a large sample, obtaining spectra will not be possible for all objects and photometrically derived redshifts will therefore remain important classifiers. Furthermore, sampling the temporal variability of quasars photometrically enables the study of the physical nature of these objects (Schmidt et al. 2011).

The spectral energy distribution of a typical quasar is marked by several prominent emission features including Lyman α in the UV and Hα emission at redder wavelengths. In Figure 22 we show how these and other prominent emission features shift with redshift causing them to overlap with absorption features due to water vapor in Earth's atmosphere. Due to the large flux contribution by these emission features in a given photometric band, when the features align with Earth's atmospheric absorption there is the potential for a significant error in the zero point correction that will be a function of the PWV during the observation.

To quantify the error in the photometry of a typical quasar spectrum, we use the composite quasar spectrum described in Berk et al. (2001). This spectrum was generated by averaging together over
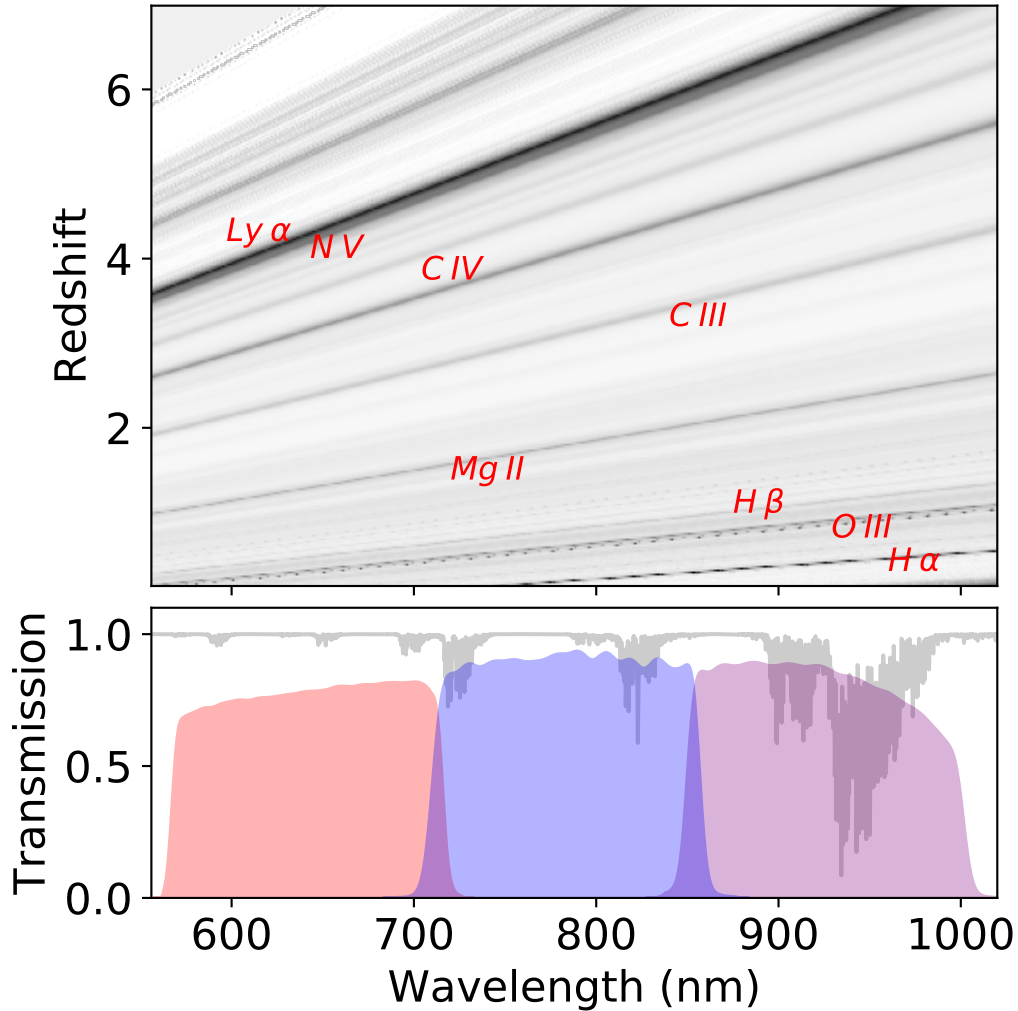
Figure 22. (top) Quasar spectra at different redshifts with prominent emission lines and (bottom) telluric spectra and r, i, and z MzLS filter profiles.

2000 SDSS spectra to provide a high SNR spectrum that is characteristic of a typical quasar spectrum and covers a wide restframe wavelength range of 80–855 nm. Using the TAPAS telluric transmission spectrum and this composite spectrum, we compute the change in magnitude in r, i, and z passbands and compare it to the extinction in a K9 reference star in the same atmospheric conditions. We compute this error term on a redshift grid ranging from 0.15 to 3. The error in r is less than 1 mmag at all values of redshift and PWV, while the i and z bands have errors as high as 15 and 60 mmag, respectively, for the highest PWV of 15 mm. Figure 23 shows the full effect for σ_i and σ_z in grids of redshift and PWV. As expected, the largest errors are observed when spectral features overlap with absorption in Earth's atmosphere. Quasars at z 0.4 have the highest error due to Hα overlapping the strong 940 nm water vapor band.
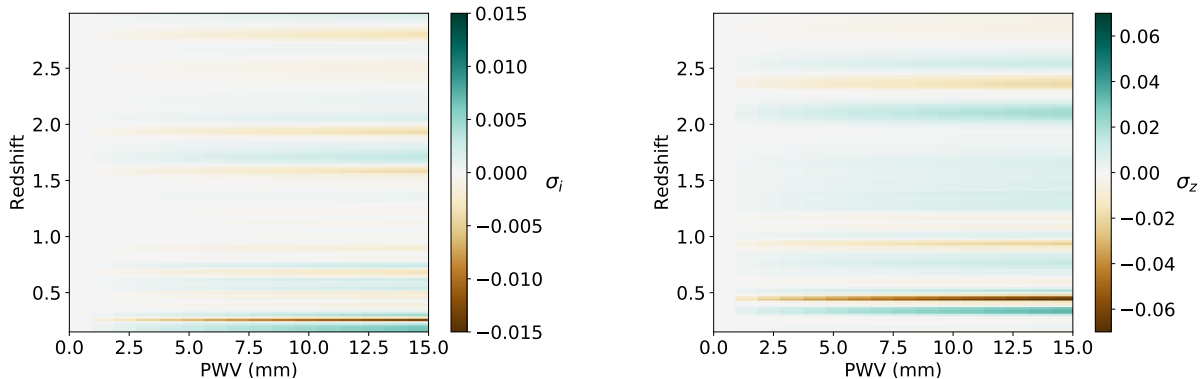
Figure 23. Error in the i band (left) and z band (right) of a composite quasar at various redshifts and PWV values.

Quasars vary in brightness on time scales from hours to years (Ulrich et al. 1997; Vanden Berk et al. 2004; de Vries et al. 2005; Kimura et al. 2020). While 20–60 mmag changes in z are quite small with respect to the long-term intrinsic variability of quasars, on short time scales, the PWV-induced variability can be greater than the short-term intrinsic variability of quasars. If the cadence of observations is high enough and the PWV during observations is known, this absorption could help constrain the redshift of an object. Other efforts to utilize the effects of Earth's atmosphere to aid photometric redshift estimates include the works by Graham et al. (2018) and Kaczmarczik et al. (2009). In Kaczmarczik et al. (2009), the authors show how atmospheric refraction causes objects with different SEDs to experience different positional offsets, which can help break the degeneracies in photometric redshift estimates. The authors therefore suggest that surveys like LSST observe several frames of a part of the sky at high airmass to increase the magnitude of the differential chromatic refraction between survey objects. Graham et al. (2018) also show how higher airmass observations can produce changes in an object's magnitude that is a function of the object type. Since water vapor absorption is variable in time, looking for correlations between the z magnitudes (or LSST y) with PWV in time would further aid in breaking degeneracies.

The PWV-induced errors in quasar color may also be pertinent to studies monitoring the color variability of these objects. This added scatter in the r and z bands should be noted in such an analysis for quasars at redshifts that maximize the color error. Because quasars are prevalent throughout the sky, another use of this effect could be to generate a sample of quasars at redshifts leading to overlap with prominent spectral features that can then be used to track changes in PWV. For this to work, many quasars would need to be monitored to average down their intrinsic variability in order to reveal their common mode variability due to changing PWV. Wide-field surveys such as LSST may observe sufficient quasars in one exposure to identify the common-mode variability.

6. DISCUSSION AND CONCLUSIONS

The dominant effect in zero-point variation in MzLS was a long-term secular trend that was not correlated with either the GPS-measured PWV or with the observed color-dependent relative brightness of observed stars. This secular trend was thus consistent with uniform loss of sensitivity across the z passband. We use independently measured PWV values through a dual-band GPS system was to successfully model much of the remaining variation.

In principle, the effect of PWV should be determinable from the differential change in magnitude between stars of different spectral types. In practice, we found that PWV measurements from the dual-band GPS system at KPNO did a significantly better job of predicting z-band zero-point variation than using the differential change in brightness of stars of different spectral types. Further more, the dual-band GPS-measured PWV allowed us to successfully correct the observed stellar-color-dependent errors along with the explaining the non-secular zero-point variations.

Despite its non-smooth nature, PWV absorption can be reasonably well-accounted for in a simple linear treatment for SEDs that are smooth. Specifically, the difference is very small for O–K stars because the SEDs of these stars are well-approximated as smooth blackbodies and z-band is on the Rayleigh-Jeans self-similar tail for these objects. However, the difference is noticeable for M dwarfs and more so for even cooler stars both because the SED becomes non-monotonic within the z band pass as the peak shifts through the band pass and because as molecules start to form in the stellar atmosphere the SED deviates noticeably from that of a blackbody. This difference has more significant consequences when observing objects with non-stellar SEDs across of range of redshifts, such as supernovae and quasars. In addition, for time-domain science with strict requirements on accuracy and precision, such as SN Ia cosmology or exoplanet characterization around M dwarfs, a dual-band GPS system can provide more precise measurements of PWV on a per-observation basis.

An ideal calibration system would utilize all four of the following complementary methods: (1) large-scale forward-modeling of repeated visits; (2) narrow-band imaging of stars; (3) contemporaneous stellar spectra; and (4) dual-band GPS measurements. Reliance on a single method is high-risk and will result in uncalibrated data with a method fails. Relying on just two methods means you use one to calibrate and the second to check; what do you do when they disagree? Having three or more different methods available allows for a more robust determination with the ability to identify aberrations in any one particular method.

The FGCM model used in DES Y3A1 calibration successfully took advantage of #1 and #4. Future DES calibrations should be able to add in data from aTmCAM (Li et al. 2014) and provide a comparison of the two different auxiliary methods of determining PWV.

The list is not precisely parallel. While #2–4 are distinct methods with different instrumentation, #1 is an analysis approach: a forward modeling approach can be used not just for the main survey science data, but could also make use of information from #2–4 by including those results as data that the forward model could either incorporate or seek to explain.

We recommend that astronomical observatories install and keep dual-band GPS monitoring systems at observatories. Large surveys may eventually have enough repeated measurements to calibrate out PWV absorption for the stellar population, and with a forward-modeling approach potentially for more general SEDs. But even the calibration of the DES Y3 data, which had ample multi-epoch and multi-filter data, was clearly improved by using independently measured PWV from auxiliary sources. Smaller programs, or single-pass surveys, are less able to make such corrections. A dual-band GPS system is inexpensive and provides specific and accurate information about the PWV impact on atmospheric transmission.

ACKNOWLEDGMENTS

APPENDIX

A. CCD TEMPERATURE VARIATION WAS NOT A SOURCE OF SIGNIFICANT ZERO POINT VARIATION

CCD temperatures can have a significant effect on the z-band QE. See Groom et al. (2017) for a detailed discussion of the transmissions for these thick CCD sensors used in Mosaic-3. As we approach the Si band-gap energy, single- and double-phonon-assisted conversion of photons becomes at first a significant and then the dominant source of promotion of electrons into the conductance band. We thus additionally look at CCD temperatures for the z-band variations from MzLS.

Figure 24 shows the CCD temperatures for the Mosaic-3 camera over the course of the MzLS survey. Each CCD stayed within 2 C of its typical temperature over the course of the the MzLS survey (see Table 3), with the exception of 6 outlier nights. We compiled these data by extracting the CCDTEMP1,2,3,4 values from the FITS file headers of the files on disk at NERSC.

There are six nights in the survey where the CCD temperatures were significant outliers. See Table 4. There is one night when the CCD temperatures were at < -125 C. There are five more nights when the CCD temperatures were at < -110 C. There is no significant zero-point dependency detectable on these nights, it does not noticeably affect the variance of (MJD, PWV)-corrected ZPT.

REFERENCES

Abbott, T. M. C., Allam, S., Andersen, P., et al. 2019, ApJL, 872, L30

Baker, A. D., Blake, C. H., & Sliski, D. H. 2017, PASP, 129, 85002

Table 3. MzLS CCD Median Temperature

CCD	Median temperature [C]
1	-101.375
2	-104.332
3	-105.316
4	-103.593

Table 4. MzLS CCD Temperature Outlier Nights

Observing Night [MST][a]	MJD	T [C]
2016-04-25	57504	-125 − -142
2016-04-26	57505	-110 − -112
2016-05-10	57519	-110 − -125
2016-05-30	57539	-110 − -112
2017-04-20	57864	-110 − -112
2017-08-03	57969	-110 − -120

[a]UTC is 6 hours ahead of MST, and the Observing Night is defined as the local date at the start of the evening, so the MJD above is for the next UTC date.

Berk, A., Conforti, P., Kennett, R., et al. 2014, Proc. SPIE, 9088, 9088

Berk, D. E. V., Richards, G. T., Bauer, A., et al. 2001, The Astronomical Journal, 122, 549

Bertaux, J. L., Lallement, R., Ferron, S., Boonne, C., & Bodichon, R. 2014, A&A, 564, A46

Betoule, M., Kessler, R., Guy, J., et al. 2014, A&A, 568, A22

Bevis, M., Businger, S., Chiswell, S., et al. 1994, Journal of Applied Meteorology, 33, 379

Bevis, M., Businger, S., Herring, T. A., et al. 1992, Journal of Geophysical Research: Atmospheres, 97, 15787

Blake, C. H., & Shaw, M. M. 2011, Publications of the Astronomical Society of the Pacific, 123, 1302

Braun, J., & Hove, T. 2001, in Proceedings of the 18th International Technical Meeting of the Satellite Division of The Institute of Navigation

Buehler, S. A., Östman, S., Melsheimer, C., et al. 2012, Atmospheric Chemistry and Physics, 12, 10925

Burke, D. L., Axelrod, T., Blondin, S., et al. 2010, The Astrophysical Journal, 720, 811

Burke, D. L., Saha, A., Claver, J., et al. 2014, The Astronomical Journal, 147, 19

Burke, D. L., Rykoff, E. S., Allam, S., et al. 2018, AJ, 155, 41

Burleigh, K. J., Landriau, M., Dey, A., et al. 2020, arXiv e-prints, arXiv:2002.05828

Dark Energy Survey Collaboration, Abbott, T., Abdalla, F. B., et al. 2016, MNRAS, 460, 1270

de Vries, W. H., Becker, R. H., White, R. L., & Loomis, C. 2005, AJ, 129, 615

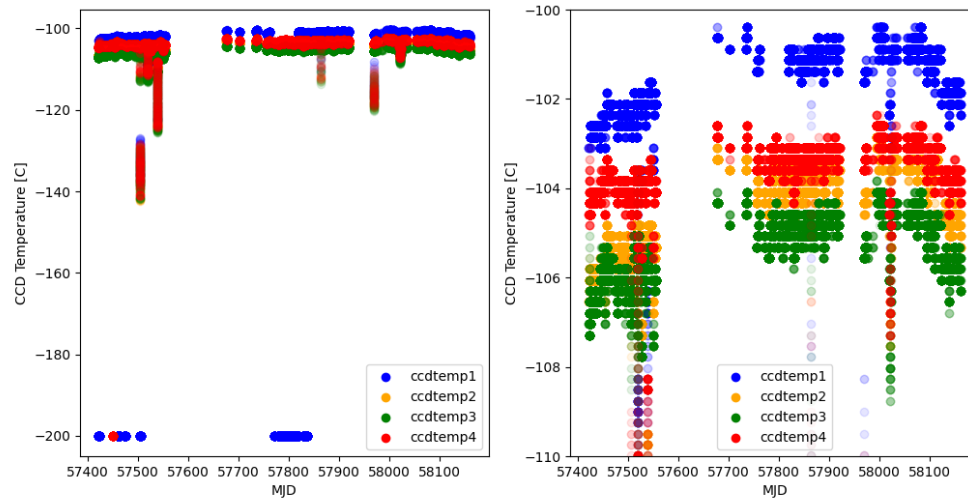Dey, A., & Valdes, F. 2014, Publications of the Astronomical Society of the Pacific, 126, 296

Figure 24. The CCD temperatures over the two years of the survey. Variation was about 2 C for each CCD, and each CCD had an ∼1 C offset with respect to the other CCDs. (left) full temperature range – note the 6 outlier nights (the first two nights appear together on this plot). (right) zoom on the typical range during the survey. The discreteness in the temperature measurements is due to a 0.246 C step size in the digitization of the signal. We interpret the recorded values at -200 C as anomalous.

Dey, A., Rabinowitz, D., Karcher, A., et al. 2016, Society of Photo-Optical Instrumentation Engineers (SPIE) Conference Series, Vol. 9908, Mosaic3: a red-sensitive upgrade for the prime focus camera at the Mayall 4m telescope, 99082C

Dey, A., Schlegel, D. J., Lang, D., et al. 2019, AJ, 157, 168

Dumont, D. M., & Zabransky, J. 2001, in Proceedings of the Eleventh Symposium on Meteorological Observations and Instrumentation, 245–247

Flaugher, B., Diehl, H. T., Honscheid, K., et al. 2015, AJ, 150, 150

Graham, M. L., Connolly, A. J., Ivezić, Ž., et al. 2018, AJ, 155, 1

Groom, D. E., Haque, S., Holland, S. E., & Kolbe, W. F. 2017, Journal of Applied Physics, 122, 055301

Guy, J., Astier, P., Baumont, S., et al. 2007, A&A, 466, 11

Hagemann, S., Bengtsson, L., & Gendt, G. 2003, Journal of Geophysical Research: Atmospheres, 108, doi:10.1029/2002JD003235

Husser, T. O., Wende-von Berg, S., Dreizler, S., et al. 2013, A&A, 553, A6

Ivezić, Ž., Smith, J. A., Miknaitis, G., et al. 2007, The Astronomical Journal, 134, 973

Ivezić, Ž., Kahn, S. M., Tyson, J. A., et al. 2019, ApJ, 873, 111

Kaczmarczik, M. C., Richards, G. T., Mehta, S. S., & Schlegel, D. J. 2009, The Astronomical Journal, 138, 19

Kimura, Y., Yamada, T., Kokubo, M., et al. 2020, ApJ, 894, 24

Lasker, J., Kessler, R., Scolnic, D., et al. 2019, MNRAS, 485, 5329

Li, D., Blake, C. H., Nidever, D., & Halverson, S. P. 2017, Publications of the Astronomical Society of the Pacific, 130, 14501

Li, T., DePoy, D. L., Marshall, J. L., et al. 2014, Society of Photo-Optical Instrumentation Engineers (SPIE) Conference Series, Vol. 9147, Monitoring the atmospheric throughput at Cerro Tololo Inter-American Observatory with aTmCam, 91476Z

Li, T. S., DePoy, D. L., Marshall, J. L., et al. 2016, The Astronomical Journal, 151, 157

LSST Science Collaboration, Abell, P. A., Allison, J., et al. 2009, arXiv e-prints, arXiv:0912.0201

Magnier, E. A., Schlafly, E. F., Finkbeiner, D. P., et al. 2016, arXiv e-prints, arXiv:1612.05242

Manandhar, S., Lee, Y. H., Meng, Y. S., Yuan, F., & Dev, S. 2018, arXiv e-prints, arXiv:1805.01961

Moore, A. W., Small, I. J., Gutman, S. I., et al. 2015, Bulletin of the American Meteorological Society, 96, 1867

Nahmias, M. H., & Zabransky, J. 2004, BAMS

Perlmutter, S., Aldering, G., Goldhaber, G., et al. 1999, ApJ, 517, 565

Perrefort, D., Wood-Vasey, W. M., Bostroem, K. A., et al. 2019, PASP, 131, 25002

Richards, G. T., Myers, A. D., Gray, A. G., et al. 2009, ApJS, 180, 67

Riess, A. G., Filippenko, A. V., Challis, P., et al. 1998, AJ, 116, 1009

Sapucci, L. F., Machado, L. A. T., de Souza, E. M., & Campos, T. B. 2019, Meteorological Applications, 26, 49

Schindler, J.-T., Fan, X., Huang, Y.-H., et al. 2019, The Astrophysical Journal Supplement Series, 243, 5

Schlafly, E., Finkbeiner, D. P., & Juric, M. 2012, in American Astronomical Society Meeting Abstracts, Vol. 219, American Astronomical Society Meeting Abstracts #219, 428.16

Schmidt, K. B., Rix, H.-W., Shields, J. C., et al. 2011, The Astrophysical Journal, 744, 147

Scolnic, D. M., Jones, D. O., Rest, A., et al. 2018, ApJ, 859, 101

Shangguan, M., Heise, S., Bender, M., et al. 2015, Annales Geophysicae, 33, 55

Stubbs, C. W., High, F. W., George, M. R., et al. 2007, Publications of the Astronomical Society of the Pacific, 119, 1163

Tie, S. S., Martini, P., Mudd, D., et al. 2017, AJ, 153, 107

Tralli, D. M., & Lichten, S. M. 1990, Bulletin Geodesique, 64, 127

Ulrich, M.-H., Maraschi, L., & Urry, C. M. 1997, ARA&A, 35, 445

Vanden Berk, D. E., Wilhite, B. C., Kron, R. G., et al. 2004, ApJ, 601, 692

Wade, R. A., & Horne, K. 1988, ApJ, 324, 411

Ware, R. H., Fulker, D. W., Stein, S. A., et al. 2000, Bulletin of the American Meteorological Society, 81, 677